Photoionization from the Xe 4d orbitals of XeF2

R. Forbes, P. Hockett, I. Powis, J. D. Bozek, D. M. P. Holland, and S. T. Pratt

Published version information

Citation: R Forbes et al. Photoionization from the Xe 4d orbitals of XeF2. J Chem Phys 155, no. 19 (2021): 194301

DOI: 10.1063/5.0068530

The Journal of Chemical Physics

Photoionization from the Xe 4d orbitals of XeF_2

Cite as: J. Chem. Phys. **155**, 194301 (2021); https://doi.org/10.1063/5.0068530
Submitted: 25 August 2021 • Accepted: 26 October 2021 • Published Online: 18 November 2021

R. Forbes, P. Hockett, I. Powis, et al.

The Journal of Chemical Physics ARTICLE scitation.org/journal/jcp

Photoionization from the Xe 4d orbitals of XeF_2

Cite as: J. Chem. Phys. 155, 194301 (2021); doi: 10.1063/5.0068530
Submitted: 25 August 2021 • Accepted: 26 October 2021 •
Published Online: 18 November 2021

R. Forbes,[1] P. Hockett,[2] I. Powis,[3] J. D. Bozek,[4] D. M. P. Holland,[5] and S. T. Pratt[6,a)]

AFFILIATIONS

[1] Stanford PULSE Institute, SLAC National Accelerator Laboratory, 2575 Sand Hill Road, Menlo Park, California 94025, USA
[2] National Research Council of Canada, 100 Sussex Dr., Ottawa, Ontario K1A 0R6, Canada
[3] School of Chemistry, University of Nottingham, Nottingham NG7 2RD, United Kingdom
[4] Synchrotron SOLEIL, l'Orme des Merisiers, Saint-Aubin, BP 48, 91192 Gif-sur-Yvette, France
[5] Daresbury Laboratory, Daresbury, Warrington, Cheshire WA4 4AD, United Kingdom
[6] Chemical Sciences and Engineering Division, Argonne National Laboratory, Lemont, Illinois 60439, USA

[a)] **Author to whom correspondence should be addressed:** stpratt@anl.gov

ABSTRACT

We present a comparison of the photoionization dynamics of the 4d shell of XeF_2 from threshold to 250 eV to those of the prototypical 4d shell of atomic Xe. The new experimental data include spin–orbit and ligand-field-resolved partial cross sections, photoelectron angular distributions, branching fractions, and lifetime widths for the 4d-hole states. The spin–orbit branching fractions and angular distributions are remarkably similar to the corresponding distributions from atomic Xe across a broad energy interval that includes both the intense shape resonance in the f continuum and a Cooper minimum in the same channel. The angular distributions and branching fractions are also in reasonably good agreement with our first-principles theoretical calculations on XeF_2. Data are also presented on the lifetime widths of the substate-resolved 4d-hole states of XeF_2. While the trends in the widths are similar to those in the earlier experimental and theoretical work, the linewidths are considerably smaller than in the previous measurements, which may require some reinterpretation of the decay mechanism. Finally, we present new data and an analysis of the Auger electron spectra for ionization above the 4d thresholds and resonant Auger spectra for several pre-edge features.

I. INTRODUCTION

Photoexcitation and ionization from the 4d shell of atomic Xe have long been a touchstone for experimental and theoretical studies of shape resonances, Cooper minima, and interchannel coupling.[1–23] Removal of a 4d electron from Xe results in two spin–orbit states, $^2D_{5/2}$ and $^2D_{3/2}$, with thresholds of 67.548(11) and 69.537(12) eV, respectively.[5] Experiment and theory have both addressed the corresponding photoabsorption and photoionization cross sections,[1–6,13,20] photoelectron angular distributions,[9,10] and spin–orbit branching ratios.[4,18] The 4d hole states lie above the double- and triple-ionization thresholds of Xe (33.105 ± 0.004 and 64.09 ± 0.04 eV, respectively[24,25]), and the decay processes of the 4d-hole states have also been the subject of intense study, with determinations of Auger decay widths,[21,22] final-state branching ratios, and Auger electron angular distributions.[15,26] Photoelectron–Auger electron coincidence and Auger electron–ion coincidence measurements have been particularly effective for characterizing the multiple decay pathways.[27–29]

The evolution of structure and dynamics from those of a free atom to those of a molecule can provide deep insight into the nature of chemical bonding, particularly when they are studied as a function of the molecular orbital—from outer-valence to inner-valence and to outer-core and inner-core orbitals. One of the most interesting questions about the outer-core electrons is the extent to which they are affected by the molecular environment and participate in molecular bonding. From this perspective, the xenon fluorides, XeF_n (n = 2, 4, and 6), represent a particularly intriguing set of relatively weakly bound molecules in which the perturbation of the Xe inner-shell electrons by the highly electrophilic fluorine ligands[30–32] can be characterized with considerable detail and benchmarked against the wealth of data on atomic Xe.

In this paper, we focus on the photoexcitation of the 4d subshell of XeF_2 between 60 and, i.e., 250 eV and on the decay of

the $4d^{-1}$ hole states. The present work builds on a long history of work on the xenon fluorides. Comes *et al.*[31] recorded the first extreme ultraviolet (XUV) photoabsorption spectrum of XeF_2 and XeF_4 between 50 and 160 eV, a region dominated by bound resonances just below the Xe $4d^{-1}$ threshold and by a large $4d \rightarrow \varepsilon f$ shape resonance in the region above it. This work was followed by photoelectron spectroscopy studies of XeF_2, XeF_4, and XeF_6 by Carroll *et al.*[32] and Bancroft *et al.*[33] at the F 1s and Xe 3d thresholds. Auger electron spectroscopy following Xe 3d hole formation was also characterized by Aksela *et al.*,[34] and most recently, Southworth *et al.*[35] performed a detailed study of the fragmentation dynamics of XeF_2 following 3d hole production. At lower energy, Cutler *et al.*[36] used high-resolution photoelectron spectroscopy to characterize the ligand-field and spin–orbit splittings of the Xe 4d hole states in XeF_2, XeF_4, and XeF_6. Cutler *et al.*[36] explained the observed ligand-field splittings with an instructive model for the bonding, and they also found different lifetime widths for the different ligand-field-split substates. Bancroft *et al.*[37] later studied the interchannel coupling among the valence continua and the 4d excitation channel between 50 and 110 eV, and found good agreement with their theoretical predictions.

The earliest theoretical work on XeF_2 was performed by Basch *et al.*[30] and was aimed at the characterization of the ordering of the molecular orbitals and the nature of the bonding. The currently accepted ordering of the configuration of XeF_2 is: $\ldots(\mathrm{Xe\,4s})^2(\mathrm{Xe\,4p})^6(\mathrm{Xe\,4d})^{10}8\sigma_g^{\,2}5\sigma_u^{\,2}9\sigma_g^{\,2}6\sigma_u^{\,2}4\pi_u^{\,4}3\pi_g^{\,4}10\sigma_g^{\,2}5\pi_u^{\,4}$.[33] More recently, Buth *et al.*[38] performed detailed calculations on the single-ionization spectra of XeF_2, XeF_4, and XeF_6 from the first ionization energy to the Xe 4d ionization threshold. In a subsequent paper,[39] they performed calculations and analysis of the double ionization thresholds and a study of the decay mechanisms for the Xe 4d hole states. One of the interesting observations of Cutler *et al.*[36] was that the Auger decay widths, Γ, of the Xe 4d hole states increased with the addition of fluorine with Xe < XeF_2 < XeF_4 < XeF_6. Buth *et al.* explained this trend in terms of an increasingly important contribution from interatomic Coulombic decay (ICD) to the Auger process. In later work, Pernpointner and Cederbaum[40] assessed the role of relativistic effects on the ionization spectra of these molecules. A second theoretical study of XeF_2 including relativistic effects was reported by Haiduke *et al.*[41]

Here, we present new ion-yield and high-resolution photoelectron spectra that result in a comprehensive dataset for the $4d^{-1}$ partial photoionization cross sections for XeF_2 and the photon-energy dependence of the XeF_2 $4d^{-1}$ substate branching fractions and photoelectron angular distributions. These data are compared with the earlier results, as well as with new theoretical calculations, and with the vast data on atomic Xe. The photoelectron spectra also allow for a more detailed examination of the substate-specific widths and Auger decay lifetimes for the XeF_2 $4d^{-1}$ hole and for a more detailed comparison with theory. Auger electron and resonant Auger electron spectra are also reported that provide additional insight into the decay mechanisms of the $4d^{-1}$ hole. This study complements our recent comparisons of the 3d and 4d photoexcitation of Xe and methyl iodide, CH_3I, a more strongly bound system that is isoelectronic with Xe.[42,43]

In what follows, the experimental and theoretical methodologies are described first, followed by a presentation of the experimental data. The discussion begins with the ion-yield spectra and partial cross sections and continues on to the $4d^{-1}$ ligand-field and spin–orbit dependent branching fractions and photoelectron angular distributions. The $4d^{-1}$ substate-dependent Auger lifetime widths are then discussed. The Auger electron spectra and resonant Auger electron spectra are then discussed using insights from the calculations of Buth *et al.*[38,39] Finally, the present findings are discussed in the context of the growing number of pump–probe experiments performed by using new ultrafast sources of XUV and x-ray radiation.

II. EXPERIMENT

The experiments were performed on the PLEIADES beamline at the Synchrotron SOLEIL. The experimental approach was similar to that of our previous studies of the I 4d subshell of CH_3I[43] and is described only briefly here. The linearly polarized radiation from the Apple II undulator was passed through a modified Petersen monochromator and into the interaction region of a VG Scienta R4000 electron spectrometer. The undulator radiation was determined to be >99% plane polarized, and the plane was rotated to be either parallel or perpendicular to the entrance axis of the electron spectrometer. We refer to the electron signal in these two geometries as I_0 and I_{90}, respectively. The incident monochromatic photon intensity was measured with a photodiode mounted downstream of the electron spectrometer.

The major change to the experimental setup compared to that employed previously[44] was the replacement of the standard Scienta ionization cell with the one designed in-house, allowing a significantly reduced pumping capacity and, hence, sample throughput. A schematic diagram of the interaction region is included in the supplementary material. The ion yield spectra were measured in a separate chamber where the sample was introduced into the interaction region as an effusive jet through a needle positioned ~1 mm above the photon beam. A Channeltron with a 2 cm opening was positioned ~1 cm from the intersection of the two beams in the horizontal plane. The front of the Channeltron was biased with −2000 V, effectively extracting all positive photoions created in the interaction region. The ion signal from the Channeltron was amplified, discriminated, and counted for a set dwell time of 1 s per point. The inlet system for the XeF_2 sample was modified to minimize the distance between the sample holder and the ionization cell. The inlet line was extensively passivated to minimize the contribution of atomic Xe to the electron signal. The residual lines from atomic Xe could be used to calibrate both the photon energy and the electron kinetic energy. In addition, a series of photoelectron spectra was recorded using a mixed sample with roughly equal pressures of XeF_2 and Xe. While the emphasis of our measurements was on electron spectroscopy, the total ion yield spectra were also recorded for XeF_2. These spectra were used to choose the photon energies for the resonant Auger studies.

Photoelectron spectra of XeF_2 were recorded at photon energies between ~60 and 250 eV, resulting in electrons with energies of up to 240 eV. Most of the measurements focused on the $4d^{-1}$ photolines, although spectra were also recorded at selected energies to observe electrons produced by shake-up processes, Auger decay, resonant Auger processes, and valence-shell photoionization. All of the spectra have been corrected for the transmission function of

the electron spectrometer. The monochromator and electron spectrometer resolutions were optimized for the different measurements depending on the signal levels and the achievable signal-to-noise level.

In the electric dipole approximation with plane-polarized light, the differential partial cross section is given by[45]

$$\frac{d\sigma}{d\Omega} = \frac{\sigma}{4\pi}[1 + \beta P_2(\cos\,\theta)], \tag{1}$$

where σ is the angle-integrated partial cross section, β is the angular distribution parameter that takes values between −1 and 2, $P_2(\cos\theta)$ is the second-order Legendre polynomial, and θ is the angle between the plane of polarization and the plane of the ejected electron momentum. Using Eq. (1) to express β in terms of the measurements at 0° and 90°, one finds the following:

$$\beta = \frac{2(I_0 - I_{90})}{(I_0 + 2I_{90})}, \tag{2}$$

which is used in the present determinations. The entrance slit of the analyzer limits the acceptance angle in the dispersive direction, which is the relevant angle for β measurements. Taking into account the geometry of the instrument, the size and curvature of the slits, and the magnifying effect of the spectrometer lens, the angular acceptance in the measurement is ~0.5°, which results in a contribution to the uncertainty of ~1% to 2%.

A. Fitting

The photoelectron spectra of the XeF_2 $4d^{-1}$ photolines were fitted to extract the substate binding energies, peak intensities and widths, and β parameters. As described in detail previously,[42–44] a weighted nonlinear least-squares procedure was used to fit the five components (three for $4d_{5/2}{}^{-1}$ and two for $4d_{3/2}{}^{-1}$) for the $4d^{-1}$ hole. In the case of the Xe + XeF_2 mixtures, the two Xe $4d^{-1}$ lines and five XeF_2 were all fit simultaneously. The error bars derived from the fits represent only the counting statistics and do not include systematic errors. As discussed by Cutler *et al.*,[36] vibrational excitation in the $4d^{-1}$ hole spectra is expected to be a minor process, and no vibrational structure was considered. The procedure involved the simultaneous fitting of the photoelectron spectra obtained with both parallel and perpendicular polarizations with respect to the entrance slit of the electron spectrometer. In addition, at each photon energy, an experimental broadening parameter was used for all five (or seven) transitions that took into account the electron spectrometer resolution, photon bandwidth, and Doppler broadening. In contrast with our previous studies,[42–44] all five photoelectron peak widths were allowed to vary separately. The output of the fits thus provided the ligand-field- and spin–orbit-split substate-specific angular distribution parameters, peak intensities, and linewidths that form the basis for the discussion of the $4d^{-1}$ photoionization processes and decay mechanisms.

B. Computational methods

The electronic structure was computed, at the HF/SPKrQZP level, in Gamess (version 2018 R3),[46,47] and converged to an equilibrium bond length of 1.9373 Å, slightly shorter than the experimental gas-phase value of 1.977(15) Å obtained via high-resolution spectroscopy.[48] Scattering calculations made use of the ePolyScat suite,[49–51] which computes the fixed-nuclei scattering wavefunction via a Schwinger variational procedure. Although the calculations were performed in D_{8h} symmetry, here we use the corresponding $D_{\infty h}$ labels appropriate for XeF_2. Orbitals 21–25 correspond to the Xe(4d) core levels and comprise a single Σ_g orbital (oriented along the bond) and two doubly degenerate orbitals Π_g and Δ_g. The orbital energies were computed to be Σ_g = −76.58, Π_g = −76.27, and Δ_g = −75.67 eV, respectively, which is ~6 eV from our experimentally measured ligand-field-averaged energy for the lower spin–orbit component of ~70.38 eV (~72.39 eV for the upper spin–orbit component). To allow for the bond length dependence of the scattering (see, for example, Refs. 52–55) and to (crudely) approximate symmetric stretching vibrational effects, the results were computed for a range of Xe–F bond lengths about the equilibrium value, and averaged over these via a Gaussian convolution kernel with s = 0.2 Å. No treatment for the symmetry-breaking bend and asymmetric stretching was applied, although due to its low frequency the former is likely to be thermally excited in our room-temperature measurements. Full computational results and additional notes and analysis are available online via Ref. 56.

It is of note that the present calculations do not include multi-electron effects such as the Xe 4d → εf giant resonance.[57] As a result, the broad width of the resonances near 100 eV in Xe and XeF_2 is not reproduced in the ePolyScat results. An illuminating comparison can be found in Ref. 58, where multi-electron effects are investigated using a relativistic random-phase approximation (RRPA) treatment, and good agreement with the observed absolute cross sections is obtained for a range of isoelectronic atoms. Previous studies on atomic Xe have also shown that calculations including final-state correlation peaked at an energy somewhat above the experiment but reproduced the width of the resonance reasonably well.[2,56]

Spin–orbit effects were added to the computational results by introducing an additional spin–orbit coupling term that describes the final ionic states, as has been demonstrated in previous work.[59,60] This approach makes use of an angular momentum coupling term, C^{SO}, defined as follows:

$$C^{SO}(L,J,S) = \begin{pmatrix} L & J & S \\ M_L & M_J & M_S \end{pmatrix}\begin{pmatrix} L & J & S \\ \Lambda & \Omega & \Sigma \end{pmatrix}, \tag{3}$$

where the notation follows Hund's case b/c, with the lab-frame (LF) projections denoted as $M_{L,J,S}$ and the molecular frame (MF) projections denoted as Λ, Ω, and Σ. The observables then include a term defined by the coherent product over coupling terms, summed over any unobserved states, ν,

$$\Xi(L,J,S) = \sum_{\nu} C^{SO}(L,J,S)C^{SO}(L',J',S'). \tag{4}$$

In the current case, this term has been applied to the ePolyScat computed matrix elements to generate the spin–orbit split bands with the use of several assumptions. First, all lab-frame M sub-levels are assumed to be equally populated, and thus the lab-frame term will not affect the relative spin–orbit states. Second, the ion states are assumed to be fully resolved so that there are no cross-terms (coherences). The quantum numbers for the $4d^{-1}$ hole state take the values L = 2, S = 1/2, and $J = L + S$, resulting in the $^2D_{5/2}$ and $^2D_{3/2}$ terms. The ligand-field split components have Λ = 0–2, corresponding to the Σ, Π, and Δ components, respectively, which

correspond to the Σ_g, Π_g, and Δ_g states of the calculations. Ω corresponds to the allowed projection terms, sub-selected to match the experimentally assigned values. Finally, no spin–orbit energy splitting is computed, and terms are assumed to be energetically ordered as in the experimental assignments. With this approach, appropriate sub-selection and multiplication of the computational cross sections, followed by renormalization, yield the effective spin–orbit branching ratios in the one-electron model.

III. RESULTS AND DISCUSSION

Figure 1 shows the photoelectron spectrum of the $4d^{-1}$ region for a mixture of Xe and XeF_2 recorded at a photon energy of 115 eV and with $\theta = 0°$, along with the results of the fitting procedure. As discussed by Cutler *et al.*,[36] the XeF_2 $4d^{-1}$ threshold shifts to ~2 eV higher energy than the corresponding atomic Xe $4d^{-1}$ thresholds. As in Xe, the XeF_2 $4d^{-1}$ threshold is split into two spin–orbit components, corresponding to the $4d_{5/2}{}^{-1}$ and $4d_{3/2}{}^{-1}$ levels. Furthermore, each of these levels is split by ligand-field interactions. Using the results from our fitting procedure, the lower $4d_{5/2}{}^{-1}$ threshold is split into $^2\Delta_{5/2}$, $^2\Pi_{3/2}$, and $^2\Sigma_{1/2}$ states with energies of 70.169, 70.404, and 70.579 eV, respectively, while the higher energy $4d_{3/2}{}^{-1}$ threshold is split into $^2\Delta_{3/2}$ and $^2\Pi_{1/2}$ states with energies of 72.219 and 72.538 eV, respectively. These ionization energies for the ligand-field split states of XeF_2 are given in Table I.

A. Ion yield spectra and partial cross sections

Figure 2(a) shows the ion yield curve between 60 and 74 eV, that is, from approximately ten eV below the XeF_2 4d thresholds

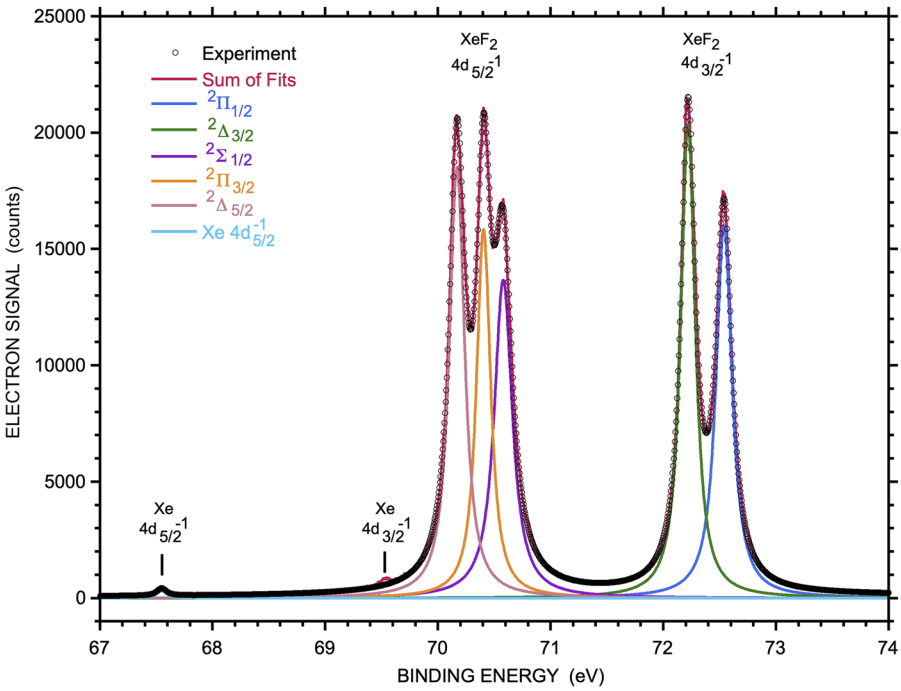

FIG. 1. The photoelectron spectrum of the $4d^{-1}$ features recorded at 115 eV with $\theta = 0°$, along with the results of the fitting procedure.

TABLE I. Average substate-dependent $4d^{-1}$ photoelectron linewidths.

Final state	Energy (eV) Present	Energy (eV) Reference 36	FWHM (eV) Present	FWHM (eV) Reference 22	FWHM (eV) Reference 36
Xe ($4d_{5/2}{}^{-1}$)	67.548(1)[a]		0.109(4)	0.111(3)	0.207(4)
Xe ($4d_{3/2}{}^{-1}$)	69.539(5)		0.102(4)	0.104(3)	0.202(4)
XeF_2 ($^2\Delta_{5/2}$)	70.169(6)	70.179(6)	0.133(7)		0.214(19)
XeF_2 ($^2\Pi_{3/2}$)	70.404(6)	70.421(9)	0.127(13)		0.256(27)
XeF_2 ($^2\Sigma_{1/2}$)	70.579(6)	70.601(13)	0.160(6)		0.264(26)
XeF_2 ($^2\Delta_{3/2}$)	72.219(6)	72.248(6)	0.123(5)		0.223(10)
XeF_2 ($^2\Pi_{1/2}$)	72.538(6)	72.568(6)	0.147(5)		0.248(8)

[a]The atomic Xe ($4d_{5/2}{}^{-1}$) energy was taken from Ref. 5 and was used to calibrate the energy scale. The absolute uncertainty in the calibration energy is 0.01 eV. The relative uncertainties for the energies of the other peaks are significantly smaller than the absolute uncertainties.

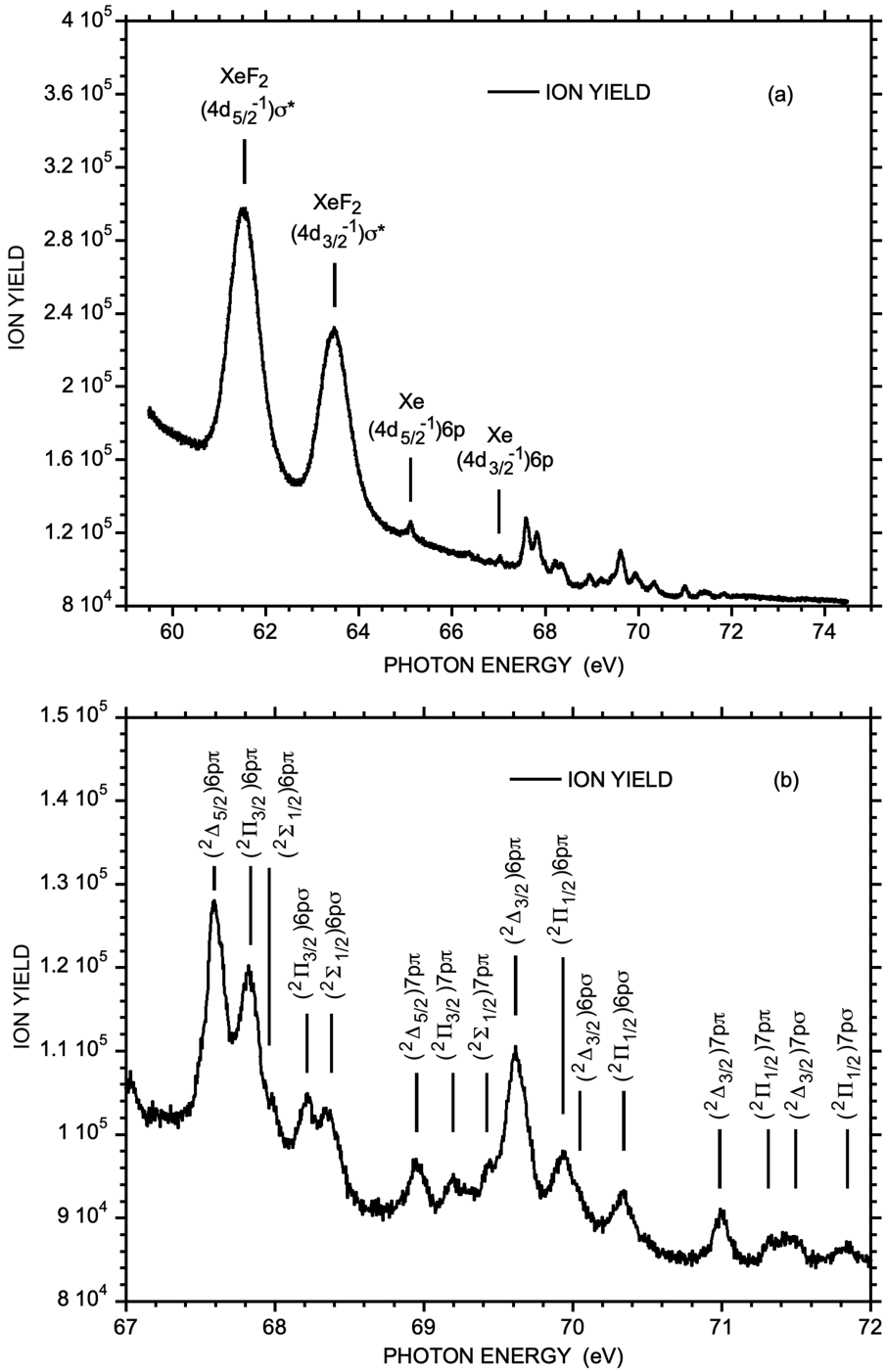

FIG. 2. (a) The total ion yield following the photoionization of XeF_2 in the region of the Xe $4d^{-1}$ ionization threshold. (b) An expanded version of the same yield highlighting the region of resonance structures between photon energies of 67 and 72 eV.

to a few eV above them. Figure 2(b) shows details of the structure between 67 and 72 eV. In Figs. 2(a) and 2(b), the ion counts were normalized to the photodiode current. The energy scale of the ion yield was calibrated by using the energy of 65.110 eV for the Xe $4d_{5/2} \rightarrow 6p$ transition.[5] The spectrum is quite similar to the photoabsorption spectrum of Comes *et al.*,[31] with some small (<0.2 eV) differences in the resonance positions, but the higher resolution (~4 meV) of the present spectrum reveals a splitting of some of the features and allows for the observation of more members of the Rydberg series. Note that because Figs. 2 and 3 (below)

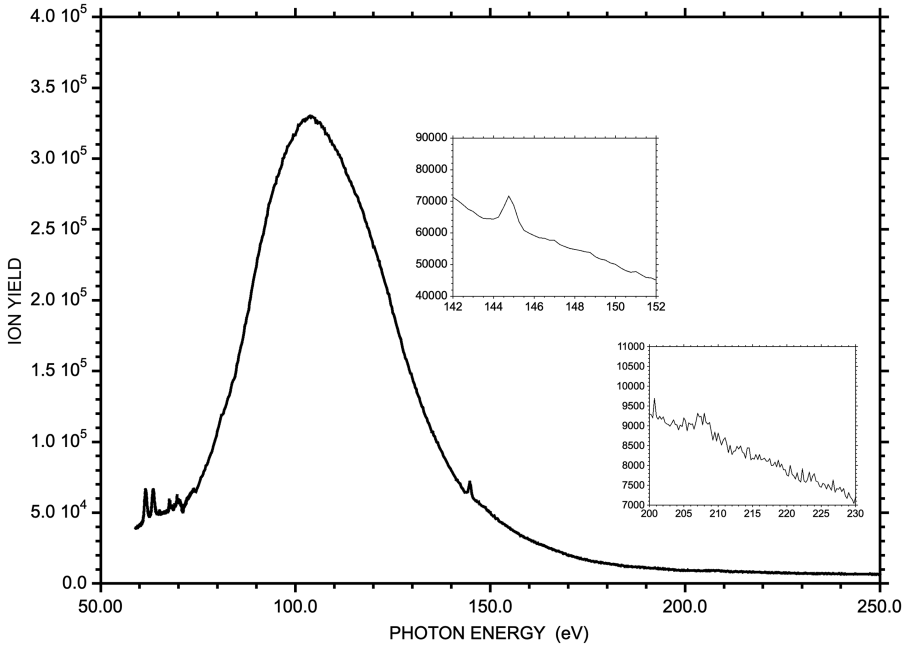

FIG. 3. The total ion yield curve following the photoionization of XeF_2 for photon energies between 60 and 250 eV. The insets show expanded versions of the resonance structures in the regions around the Xe 4p and 4s ionization thresholds.

correspond to the total ion yield, some differences with the photoabsorption spectrum are expected. In particular, photoionization followed by Auger decay or direct double photoionization produces doubly or multiply charged ions that can fragment to produce multiple counts following the absorption of a single photon. This issue is more significant above the Xe $4p^{-1}$ threshold, where direct double ionization can be substantial.[61] Nevertheless, the overall shape of the present ion yield curve matches the shape of the absorption spectrum quite well.

The two lowest energy features in Fig. 2(a) correspond to transitions from the 4d shell into the unoccupied σ_u^* valence orbital, which Comes *et al.*[31] referred to as "5p." In their model, the fluorine atoms withdraw approximately one electron each from the atomic Xe 5p orbital, leaving a partially occupied orbital into which the 4d electron can be excited. The two resonances are separated by 1.929 eV, very close to the 2.01 eV spin–orbit splitting of the XeF_2 $4d_{5/2}$–$4d_{3/2}$ multiplets, but the features are so broad that the ligand-field splittings are not observable. At higher energy, Fig. 2 shows a number of weaker features, which Comes *et al.*[31] analyzed in terms of Rydberg series converging to the five ligand- and spin–orbit-split XeF_2 $4d^{-1}$ thresholds. For excitation from the 4d shell, the dominant transitions are expected to be to the npσ and npπ Rydberg states based on these five thresholds. Comes *et al.*[31] argued that because electrons on the F atoms are more effective at screening the pσ electrons than the pπ electrons from the Xe^+ core, the pπ orbitals are expected to be more strongly bound. Excitation from the 4d orbital into the f Rydberg series is weak due to the centrifugal barrier that keeps the f electron at long range. At higher energies, the f electron penetrates the barrier, giving rise to the well-known Xe 4d-εf shape resonance in the continuum.[7]

The npσ and npπ Rydberg levels can be denoted as $[^2\Lambda^+{}_{\Omega+}]np\lambda_{\Omega e}$, Ω', where the quantity in brackets describes the $4d^{-1}$ core level and Ω' is the sum of the molecular frame projections Λ' and Σ'. The spin splitting resulting from the coupling of Ω^+ and Ω_e is small and not resolved in the present experiments. The electric dipole selection rule from the $\Omega'' = 0$ ground state of XeF_2 is $\Omega' - \Omega'' = 0, \pm 1$. Note that for the $[^2\Delta_{5/2}]np\sigma_{1/2}$ configuration, $\Omega' = 2$ or 3, both of which are forbidden from the ground state.

The model presented by Comes *et al.*[31] reproduces both the splittings and intensities of the 6pσ and 6pπ states reasonably well, and the same pattern of levels is observed in the new n = 7 states observed in the present data. As expected, however, the 7pπ–7pσ splitting is considerably smaller than the 6pπ–6pσ splitting as a result of the $1/n^{*3}$ scaling with an effective principal quantum number, n^*. Table II gives the observed transition energies, assignments based on the work of Comes *et al.*,[31] and effective principal quantum numbers calculated by using the following:

$$n^* = \sqrt{Ry/(IE - E)}, \tag{5}$$

where Ry is the Rydberg constant for XeF_2 (13.6056 eV), IE is the ionization energy, and E is the energy of the level. The n^* values can be calculated with respect to each ligand-field split threshold, and the relevant values are given in Table II. The valence shell configuration of XeF_2 is given in Table III.

While the improved resolution of the present experiments allows for the observation of additional features, the only real difference in the assignments compared with those of Comes *et al.*[31] is that they assign two weak features just below the corresponding spin–orbit split 6pπ features to transitions to the 6s Rydberg states converging to XeF_2 $4d^{-1}$. The 4d → 6s transitions are expected to be forbidden, but Comes *et al.* suggested that they become allowed by vibronic couplings. In the present spectrum, we do see the analogous features but assign them to different final states. In particular,

TABLE II. Resonance energies below the XeF_2 $4d^{-1}$ threshold.[a]

Energy (eV)[b]	Assignment	$n^*(^2\Delta_{5/2})$ 70.169 eV	$n^*(^2\Pi_{3/2})$ 70.404 eV	$n^*(^2\Sigma_{1/2})$ 70.579 eV	$n^*(^2\Delta_{3/2})$ 72.219 eV	$n^*(^2\Pi_{1/2})$ 72.538 eV	Energy (eV) (Reference 31)
61.526	$(4d_{5/2}{}^{-1})\sigma^*$	1.2547	1.2379	1.2259			61.38
63.455	$(4d_{3/2}{}^{-1})\sigma^*$				1.2460	1.2239	63.29
65.110	Xe $(4d_{5/2}{}^{-1})6p$						
66.367	Xe $(4d_{5/2}{}^{-1})7p$						
67.028	Xe $(4d_{3/2}{}^{-1})6p$						66.94 "6s"
67.596	$(^2\Delta_{5/2})6p\pi$	2.2995	2.2012	2.1357			67.49
67.820	$(^2\Pi_{3/2})6p\pi$	2.4067	2.2946	2.2207			67.73
67.983	$(^2\Sigma_{1/2})6p\pi$	2.4948	2.3706	2.2893			
68.219	$(^2\Pi_{3/2})6p\sigma$	2.6415	2.4954	2.4011			68.27
68.351	$(^2\Sigma_{1/2})6p\sigma$	2.7357	2.5743	2.4712			
68.961	$(^2\Delta_{5/2})7p\pi$	3.3560	3.1579	2.8998			69.00 "6s"
69.189	$(^2\Pi_{3/2})7p\pi$	3.7260	3.3464	3.1286			
69.433	$(^2\Sigma_{1/2})7p\pi$	4.2995	3.7433	3.4456			
69.617	$(^2\Delta_{3/2})6p\pi$				2.2867	2.1582	69.53
69.942	$(^2\Pi_{1/2})6p\pi$				2.4444	2.2893	60.84
70.029	$(^2\Delta_{3/2})6p\sigma$				2.4925	2.3287	70.20
70.338	$(^2\Pi_{1/2})6p\sigma$				2.6895	2.4868	
70.994	$(^2\Delta_{3/2})7p\pi$				3.3327	2.9685	70.89
71.328	$(^2\Pi_{1/2})7p\pi$				3.9077	3.3533	
71.472	$(^2\Delta_{3/2})7p\sigma$				4.2678	3.5736	71.47
71.822	$(^2\Pi_{1/2})7p\sigma$				5.8541	4.3592	

[a]The n^* values were calculated by using Eq. (5), the ionization energies at the top of each column, and the Rydberg constant for XeF_2 (13.6056 eV).
[b]The relative uncertainty in the line positions is 0.005 eV, and the absolute uncertainty from the calibration line is 0.01 eV.[5]

the feature at 67.028 is assigned as atomic Xe $(4d_{3/2}{}^{-1})6p$, and the feature at 68.961 is assigned as XeF_2 $(^2\Delta_{5/2})7p\pi$.

Figure 3 shows the total ion yield spectrum across a larger energy range from ~60 to ~250 eV. Unfortunately, this total ion yield is not normalized to the incident photon intensity because, over this extended energy range, the photodiode signal exhibited prominent structure due to the Si edges and to contamination. The spectrum is dominated by the 4d → εf shape resonance, and the overall appearance is very similar to that of atomic Xe, with only small differences in the peak positions and resonance width. Thus, the molecular field does not appear to have a strong effect on the ion yield from the 4d shell. In addition to the sharp resonances below 70 eV, the spectrum shows weak sharp features in the two regions shown as insets in Fig. 3. First, a small sharp feature is observed at 144.8(2) eV, with some evidence for very weak oscillations just above it. This feature is the molecular analog of the Xe 4p → 6s transition observed by Codling and Madden[62] at 141.961 eV. As in the case of the 4d resonances, the position is shifted to higher energy in XeF_2 due to the electron withdrawing characteristics of the F atoms. The second weak feature is observed at 207.8(4) eV, as compared to the XeF_2 $4s^{-1}$ threshold at 216.04 ± 0.10 eV,[33] yielding a binding energy of ~8.24 eV. Based on the binding energy of the σ_u^* valence orbital with respect to the $4d^{-1}$ threshold, the most likely assignment for the 207.8 eV feature is $4s \rightarrow \sigma_u^*$.

Figure 4(a) shows the present theoretical 4d cross section for *atomic* Xe, along with the experimental 4d cross section from the work of Becker *et al.*,[13] and the total photoionization cross section from the work of West and Morton.[6] Theoretical calculations based on the relativistic random phase approximation (RRPA) reproduce the experimental Xe cross section with very good agreement.[7] The present ePolyScat results, which were obtained using the length

TABLE III. Valence shake-up processes.

XeF_2 ground state valence configuration $\ldots 8\sigma_g{}^2 5\sigma_u{}^2 9\sigma_g{}^2 6\sigma_u{}^2 4\pi_u{}^4 3\pi_g{}^4 10\sigma_g{}^2 5\pi_u{}^4$	
$4d_g \xrightarrow{dipole} \varepsilon\ell_u$; $6\sigma_u \xrightarrow{monopole} \sigma^*$	*normal process*
$4d_g \xrightarrow{dipole} \sigma^*$; $5\pi_u \xrightarrow{monopole} \varepsilon\pi_u$	*conjugate process*
$4d_g \xrightarrow{dipole} \sigma^*$; $10\sigma_g \xrightarrow{monopole} \varepsilon\sigma_g$	*conjugate process*
$4d_g \xrightarrow{dipole} \sigma^*$; $3\pi_g \xrightarrow{monopole} \varepsilon\pi_g$	*conjugate process*
$4d_g \xrightarrow{dipole} \sigma^*$; $4\pi_u \xrightarrow{monopole} \varepsilon\pi_u$	*conjugate process*
$4d_g \xrightarrow{dipole} \sigma^*$; $6\sigma_u \xrightarrow{monopole} \varepsilon\sigma_u$	*conjugate process*
$4d_g \xrightarrow{dipole} \sigma^*$; $9\sigma_g \xrightarrow{monopole} \varepsilon\sigma_g$	*conjugate process*

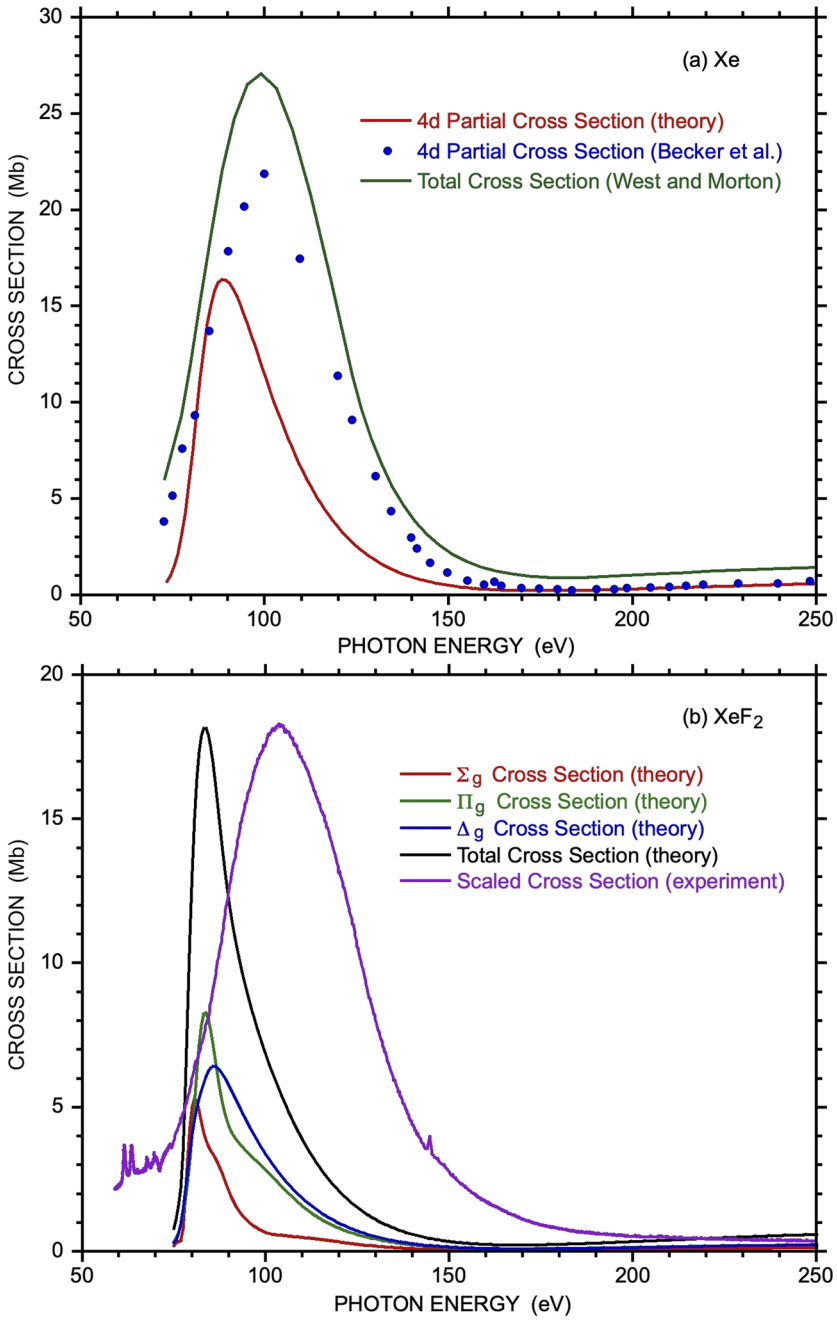

FIG. 4. (a) The present theoretical 4d partial cross section for atomic Xe, along with the experimental 4d photoionization cross section from the work of Becker *et al.*,[13] and the total photoionization cross section from the work of West and Morton.[6] (b) A comparison of the theoretical 4d cross section for XeF_2 and the present experimental data from Fig. 2. The theoretical ligand-field-split partial cross sections are also shown in the absence of spin–orbit coupling.

gauge, peak ~10 eV below the experimental energy, and the calculated resonance width is only ~60% of that for the experiment. The cross section calculated using the velocity gauge has a similar shape, but the magnitude is approximately eight times larger at its peak; this difference may be indicative of correlation effects. The differences between the present results and the more accurate results are attributed primarily to the lack of treatment of many body effects in the present calculation, as noted in Sec. II B,[57] although computational factors such as the exact form of the scattering potential will also play a role.

Figure 4(b) shows a comparison of the calculated 4d cross section for XeF_2 with the experimental data from Fig. 3. The experimental ion yield is not absolute, and it has been scaled to the maximum of the theoretical spectrum. Theoretical cross sections for the individual ligand-field split continua are also shown in the absence of spin–orbit coupling. The level of agreement is

comparable to that for atomic Xe, with the theoretical cross section peaking at lower energy and displaying a considerably smaller width than the experimental curve. Interestingly, prior to vibrational averaging, the theoretical cross sections also showed a number of continuum resonances between 80 and 90 eV that are not evident in the experimental cross section, as well as more complex low-energy behavior. Many of these features are, however, washed out in the vibrationally averaged results shown here. In earlier studies of the valence shell ionization of XeF_2, Yates *et al.*[63] and Tse[64] found strong resonant features 10–15 eV above the threshold for photoionization out of the $10\sigma_g$ and $3\pi_g$ orbitals. Tse interpreted these resonances as excitation from the F-dominated $10\sigma_g$ and $3\pi_g$ orbitals into the continuum dominated by Xe εf character.[64] In the present case, excitation occurs from the Xe 4d orbital but is likely into the analogous continuum resonances. Further details of these features remain a topic for future work, and numerical artifacts have not been fully ruled out. No such structures have been observed in the current experimental results.

We have recorded the photoelectron spectra for the $4d^{-1}$ photolines of XeF_2 from threshold to 250 eV with sufficient resolution to resolve the ligand-field and spin–orbit substates. Figure 5 shows examples of the photoelectron spectra recorded at photon energies of 120, 150, 180, and 210 eV for radiation polarized normal to the beam direction and in the planes parallel and perpendicular to the entrance axis of the electron spectrometer. These fits allow the determination of the photoelectron angular distribution parameter, β, as well as the branching fractions for the different substates. We note that below ~95 eV photon energy, post-collision interaction effects resulting from the interaction between the photoelectrons and the Auger electrons can broaden and distort the line shapes.[65–67] We have not modeled these effects here, and focus on the data between 95 and 250 eV.

Figure 6(a) shows the experimental substate-resolved β parameters for the $4d^{-1}$ photoionization of XeF_2 between 90 and 250 eV, along with the corresponding spin–orbit-resolved data for Xe. Measurements for atomic Xe have been reported previously,[10,23] and the energy dependence of the β curves is well reproduced by theory,[23,68] with the dramatic profile resulting from the shape resonance in the f continuum. The curves for the Xe^+ $4d_{5/2}$ and $4d_{3/2}$ final states are shifted slightly from each other, with some subtle differences in shape. As discussed by Wang *et al.*,[23] in the absence of dynamical effects resulting from relativistic interactions, the β parameters for the two substates should be identical when plotted vs electron kinetic energy. (When plotted vs photon energy, the $4d_{3/2}$ curve is shifted ~2 eV above the $4d_{5/2}$ curve.) The differences they observed could be explained with their calculations using the relativistic random phase approximation.[23] The present data for Xe are consistent with their measurements, but ours were not performed on as fine an energy grid.

The substate-resolved β values for XeF_2 in Fig. 6(a) are all quite similar, both to each other and to the atomic Xe data. Two small differences deserve mention. First, below ~160 eV, the β values in Fig. 6(a) for the $4d_{5/2}$ $^2\Sigma_{1/2}$ and $4d_{3/2}$ $^2\Pi_{1/2}$ substates lie noticeably below the corresponding values for the other substates. Second, above ~190 eV, the β values for the $4d_{3/2}$ $^2\Pi_{1/2}$ and $^2\Delta_{3/2}$ substates lie significantly below the other curves, and they are similar to the Xe $^2D_{3/2}$ curve. This higher energy region is also where the $Xe^+4d_{3/2}$ β curve differed more substantially from the $4d_{5/2}$ curve, an

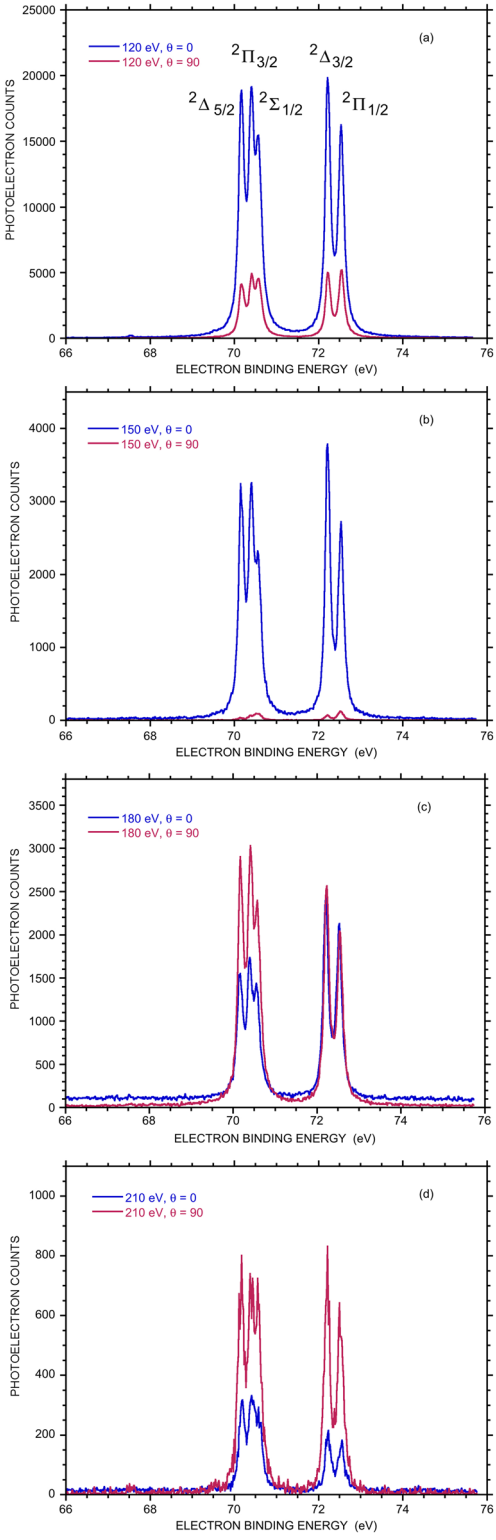

FIG. 5. Representative photoelectron spectra of the $4d^{-1}$ features recorded at (a) 120 eV, (b) 150 eV, (c) 180 eV, and (d) 210 eV with $\theta = 0°$ and 90°.

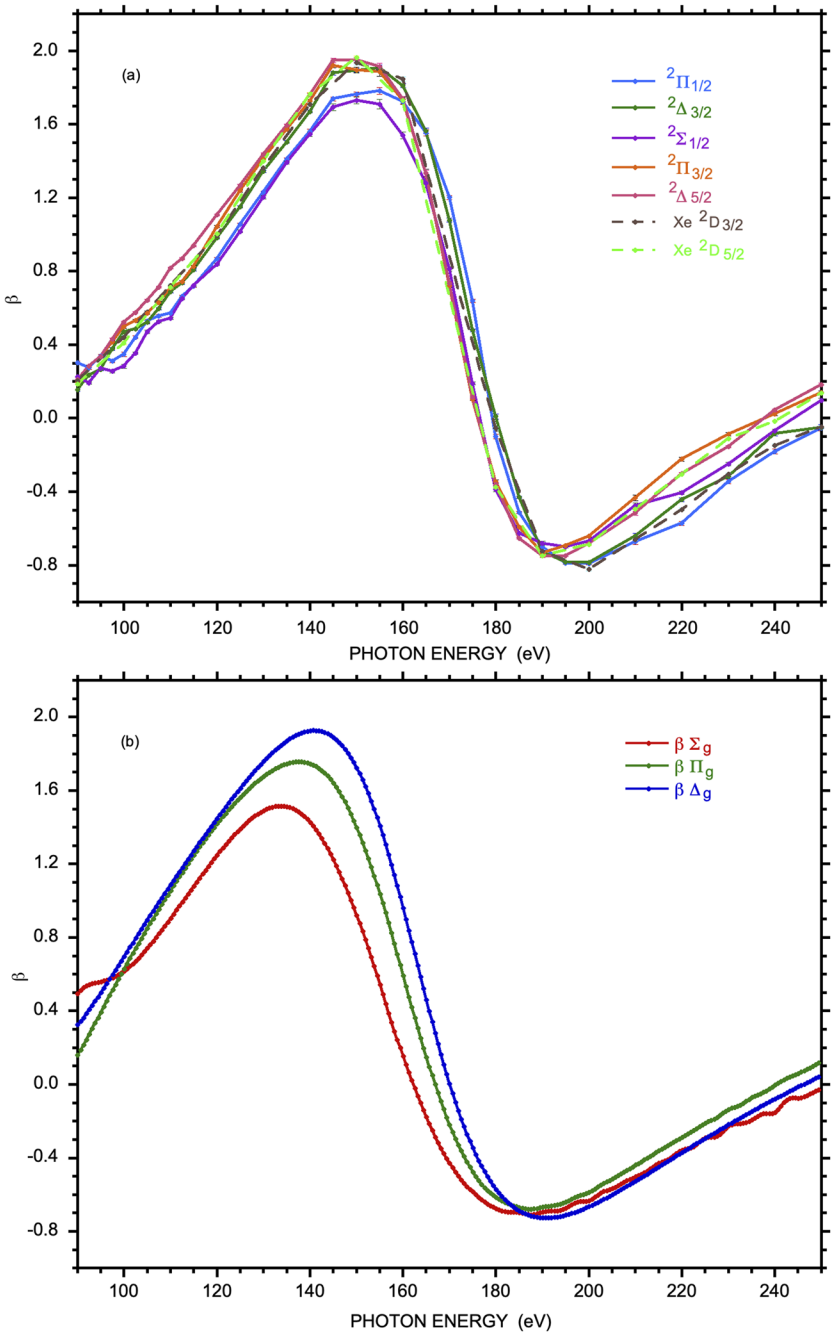

FIG. 6. (a) The substate-resolved β parameters for the photoionization of XeF_2 between 95 and 250 eV, along with the corresponding spin–orbit-resolved data on atomic Xe. (b) The theoretical ligand-field-resolved β curves in the absence of spin–orbit coupling for photoionization from the 4d shell of XeF_2.

observation that can also be made in Fig. 6(a). The present angular distribution parameters do not appear to be affected very strongly by the resonances associated with photoionization from the 4p and 4s shells, but this might simply reflect the low intensities of the resonances and the coarseness of the energy grid in Fig. 6(a).

Kukk *et al.*[69] performed a similar study of the molecular-field and spin–orbit-resolved substates of OCS^+ populated by *S* 2p photoionization. They observed significant differences in their substate-resolved angular distribution parameters relative to those given by atomic-like calculations. These differences are greatest close to threshold and reflect the molecular character of the system. At higher photoelectron energies, where the dynamics are much less sensitive to molecular effects, these effects become much smaller. The present XeF_2 data are consistent with the latter observation, with the molecular curves converging to the corresponding Xe^+ spin–orbit state curves at high energy. Unfortunately, in

the present experiment, the region close to threshold is complicated by a number of factors including shape resonances and post-collision-interaction (PCI) effects that make it difficult to calculate the molecular-field and spin–orbit dependent behavior. In addition, PCI effects will depend on the photoelectron and Auger electron angular distributions, which will be modified by resonance effects in different channels, requiring theoretical analysis beyond the scope of the present paper.

In atomic Xe, there is a Cooper minimum in the 4d → εf cross section that occurs at a photon energy of ~185(10) eV,[10,23] and this minimum is also expected in the XeF_2 4d → εf cross section. For an ionization channel generally, the observed minima in the cross section and β parameter may differ, and neither may correspond to the actual energy at which a radial dipole matrix element vanishes (this being the quantum definition for a Cooper minimum[70]) if the other non-zero matrix elements are energy dependent. Wang *et al.*[23] used the non-relativistic Cooper–Zare formula[71] for β in the 4d → εp, εf ionization to predict that, as the 4d → εf matrix element goes through zero, the photoelectron angular distribution would have $\beta = 0.2$. This equality then provides an alternative means to identify a precise energy of the Cooper minimum from a plot of the β parameter. In the relativistic case, the situation is more complicated because there are multiple continua with matrix elements that pass through zero at slightly different energies (e.g., $4d_{5/2} \rightarrow \varepsilon f_{5/2}$ and $\varepsilon f_{7/2}$). Nevertheless, Wang *et al.*[23] found that the β value corresponds to 0.2 at the average position of the minima in the two channels and that the $\beta_{5/2}$ value was 0.2 at about 2 eV lower electron kinetic energy (~4 eV lower in photon energy) than the $\beta_{3/2}$ value. In the present Xe data, the $\beta_{5/2}$ and $\beta_{3/2}$ values are 0.2 at photon energies of 174.5 and 177.3 eV, respectively (corresponding to a 0.8 eV difference in electron kinetic energy). The present values are consistent with the determinations of Lindle *et al.*[10] and Wang *et al.*[23] and are slightly lower than the position of the minimum in the total photoionization cross section (180–185 eV).[6]

In XeF_2, the situation is somewhat more complicated than in Xe because there are both spin–orbit and ligand-field splittings, and because the minima in all of the 4d → εfσ, εfπ, εfδ, and εfϕ matrix elements may occur at different energies. However, the similarities of the XeF_2 and Xe data suggest that these differences are rather small. As seen in Fig. 6(a), the XeF_2 $4d_{5/2}^{-1}$ $^2\Sigma_{1/2}$, $^2\Pi_{3/2}$, and $^2\Delta_{5/2}$ β values reach a value of 0.2 at a photon energy of 174.5 eV, the same photon energy as the Xe $4d_{5/2}^{-1}$ β value. Similarly, the XeF_2 $4d_{5/2}^{-1}$ $^2\Pi_{1/2}$ and $^2\Delta_{3/2}$ β values reach 0.2 at 177.3 eV, as does the Xe $4d_{3/2}^{-1}$ value. The XeF_2 values correspond to electron kinetic energies that are ~2.9 eV smaller than the corresponding Xe values. This difference implies that the electron withdrawing nature of the F atoms results in a slightly different energy dependence of the 4d → εf transition matrix elements.

Figure 6(b) shows the theoretical β curves for XeF_2 for the three ligand-field components in the absence of spin–orbit coupling. In contrast to the cross section calculation, the agreement with the experimental curves of Fig. 6(a) is quite good. The curves do peak at ~15 to 20 eV lower energy than the experimental ones, and their minima are shifted by a similar amount. The curve with the smallest maximum β (Σ_g symmetry) is the same as that in the experiment ($^2\Sigma_{1/2}$), and the curves with the largest β are also the same (Δ_g and $^2\Delta_{5/2}$). The β value in the Σ_g channel differs most from the atomic β curves because the $^2\Sigma_{1/2g}$ orbital along the F–Xe–F axis is the most affected by the electron-withdrawing character of the F atoms, i.e., the molecular effects. The improved agreement for the β values can be rationalized because this is primarily a single-channel response, which suggests that the scattering potential is reasonably accurate, and the scattering dynamics are described reasonably well. This observation is consistent with the previous statement (Sec. II B) that the relatively poor agreement for the cross section is likely attributed to many-body effects.

Figure 7(a) shows the $4d_{5/2}/4d_{3/2}$ spin–orbit branching ratio for XeF_2 integrated over the separate ligand-field-split states, along with the corresponding spin–orbit branching ratios for atomic Xe. The strong similarity between the two curves, even including the shallow minimum and strong rise as the photon energy approaches threshold, suggests that the spin–orbit branching ratios are largely governed by atomic effects. The detailed shape of the spin–orbit branching ratios for atomic Xe is well-reproduced by theory.[7,14,18] Above 100 eV, the branching ratio is close to the statistical value of 1.5, with only small excursions from this value of up to 250 eV.

Figure 8 shows the ligand-field-split substate branching fractions for XeF_2, where the sums of the values are separately normalized for the two spin–orbit states. For the $4d_{3/2}^{-1}$ component, the $^2\Pi_{1/2}$ and $^2\Delta_{3/2}$ branching fractions are both close to the statistical value of 0.5, with the $^2\Delta_{3/2}$ fraction being slightly larger, and there are only small variations with the photon energy. Similarly, for the $4d_{5/2}^{-1}$ component, the $^2\Sigma_{1/2}$, $^2\Pi_{3/2}$, and $^2\Delta_{5/2}$ branching fractions are all approximately equal to the statistical value of 0.33. Again, only small variations are observed as a function of photon energy.

Figure 8 also shows the results of theoretical calculations using the present model for spin–orbit coupling. Overall, the agreement with the experiment is quite good, particularly for the $4d_{3/2}$ component. However, the calculations show rather more modulations in the branching fractions, even though these are relatively small in magnitude. Although the theoretical branching fractions do show some oscillations, the lack of a stronger energy dependence in both the experimental and theoretical data seems somewhat surprising because the different ligand-field-split substates are associated with different sets of continuum partial waves, and the photoionization matrix elements show considerable variations in magnitude between 90 and 250 eV. As in the case of the β values, the reasonably good agreement between experiment and theory suggests that the branching fractions are primarily dependent on single-channel effects that are well-described by the present wavefunctions and matrix elements.

One set of photoelectron data was recorded using a mixture of Xe and XeF_2 to provide a simultaneous measurement of the $4d^{-1}$ spectra of the two species. The photoelectron data recorded with parallel and perpendicular polarization can be used to synthesize a "magic angle" photoelectron spectrum (I_m) by using the following equation:[72,73]

$$I_m = \frac{(I_0 + 2I_{90})}{3}, \tag{6}$$

in which the relative intensities of the peaks reflect the relative cross sections for the different ionization channels independent of differing angular distributions.

The integrated signals in the $4d^{-1}$ Xe and XeF_2 photoelectron peaks can be combined with the well-known absolute photoionization cross section of Xe[10,13] and the relative concentrations of Xe and

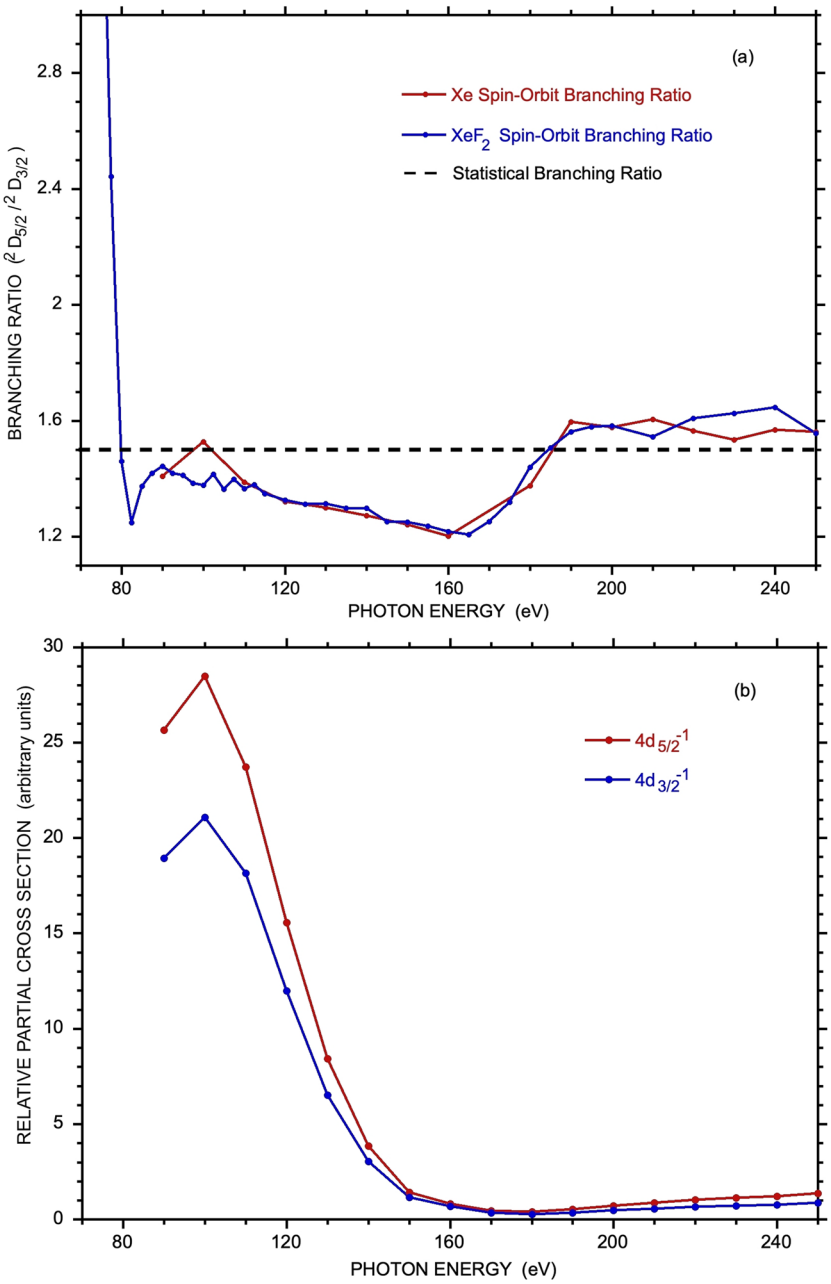

FIG. 7. (a) The $4d_{5/2}{}^{-1}/4d_{3/2}{}^{-1}$ branching ratio integrated over the ligand-field splittings for XeF_2 between the 4d threshold and 250 eV, along with the corresponding $4d_{5/2}{}^{-1}/4d_{3/2}{}^{-1}$ branching ratio for atomic Xe. (b) The experimental XeF_2 $4d_{5/2}{}^{-1}$ and $4d_{3/2}{}^{-1}$ partial cross sections determined by using Eqs. (6)–(8).

XeF_2 to yield the absolute photoionization cross sections of XeF_2,

$$\sigma_{XeF_2}(E) = \frac{N_{XeF_2}(E)\sigma_{Xe}(E)}{N_{Xe}(E)}\left(\frac{[Xe]}{[XeF_2]}\right). \quad (7)$$

Unfortunately, the relative concentrations of Xe and XeF_2 are not well-characterized, although they are expected to be relatively constant over the time of the measurement. Taking their ratio as a constant, Eq. (7) then provides a relative cross section measurement for XeF_2. This result can be further refined into XeF_2 $4d_{5/2}{}^{-1}$ and $4d_{3/2}{}^{-1}$ partial cross sections by separately integrating the two spin–orbit components of the XeF_2 signal and using

$$\sigma_{XeF_2}(4d_{5/2}^{-1}) = \frac{N_{XeF_2}(4d_{5/2}^{-1})}{N_{XeF_2}}\sigma_{XeF_2} \quad (8)$$

and the analogous equation for the $4d_{3/2}{}^{-1}$ component. The relative partial cross sections are shown in Fig. 7(b). The Cooper minima in both channels are clearly observed near 180 eV, but the energy grid is not sufficiently fine to locate them more precisely.

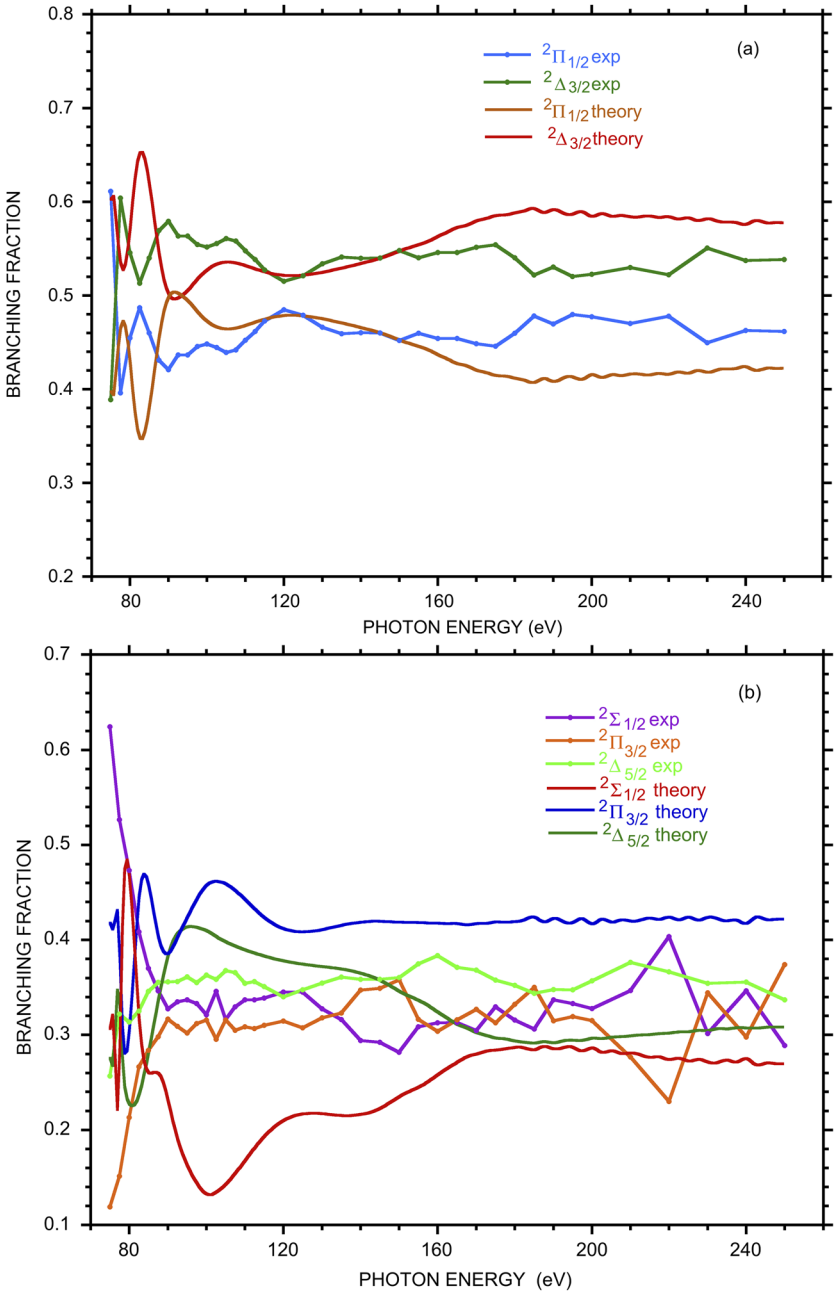

FIG. 8. The experimental ligand-field and spin–orbit-resolved branching fractions for 4d photoionization of XeF_2 between threshold and 250 eV. The corresponding theoretical branching fractions including both ligand-field and spin–orbit interactions are also shown. (a) The $4d_{3/2}^{-1}$ branching fractions. (b) The $4d_{5/2}^{-1}$ branching fractions.

B. Shake-up and shake-off spectra

Photoionization from the inner-shell orbitals is often accompanied by weaker shake-up or shake-off processes in which a second electron is excited or ejected from a valence orbital in conjunction with the ejection of the core electron.[74] Such processes typically occur in the energy region of ~5 to 25 eV above the inner-shell threshold. Although most of the present photoelectron spectra are focused on the $4d^{-1}$ main lines, photoelectron spectra over a much larger kinetic energy range were recorded at photon energies of 90, 120, and 150 eV to characterize both the shake-up and Auger processes associated with the $4d^{-1}$ photoionization of XeF_2. Tse *et al.*[75] discussed the Xe 3d and 4d shake-up processes for XeF_2 following ionization by Al Kα radiation (~1486 eV). The spectrum was not well-resolved, but at this energy, the direct/normal shake-up process is expected to dominate, and the experimental spectrum was fitted accordingly.

Figure 9 shows a portion of the photoelectron spectrum of XeF_2 recorded at 150 eV in the region of the $4d^{-1}$ shake-up and shake-off processes. The full spectrum is given in the

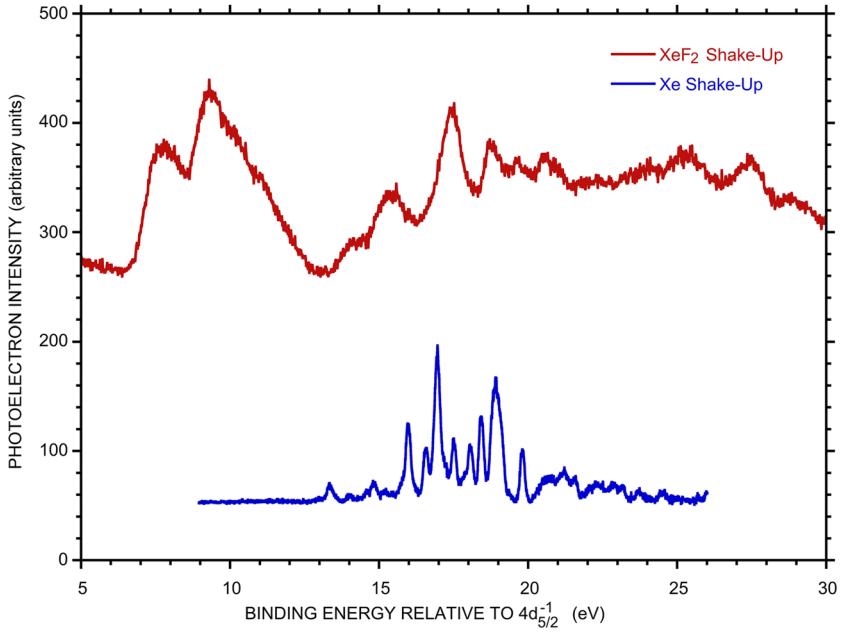

FIG. 9. A portion of the 150 eV photoelectron spectrum showing the shake-up region and plotted in terms of the excitation energy relative to the lowest Xe $4d_{5/2}^{-1}$ binding energy of XeF_2 ($^2\Delta_{5/2}$ at 70.169 eV). Also shown is the corresponding spectrum of atomic Xe from Ref. 73 and plotted relative to the atomic Xe $4d_{5/2}^{-1}$ binding energy (67.548 eV).

supplementary material. The spectrum is plotted in terms of the excitation energy relative to the lowest Xe $4d_{5/2}^{-1}$ binding energy of XeF_2 (70.169 eV). Also shown is the corresponding spectrum of atomic Xe recorded by Holland[76] and plotted relative to the atomic Xe $4d_{5/2}^{-1}$ binding energy (67.548 eV).[5] Ausmees *et al.*[19] discussed the assignment of the latter spectrum, breaking it down into sections. The weak structure at binding energies below 16 eV is not present in the spectrum recorded at a photon energy of 1487 eV, and it was assigned to conjugate shake-up processes to final states with $(4d^{-1}5p^{-1})5d$ and 6s configurations. The strong peaks at excitation energies of 16–20 eV were assigned to the normal shake-up processes to $(4d^{-1}5p^{-1})6p$ states, and at higher energy some overlap with $(4d^{-1}5p^{-1})7p$ states is expected. Unfortunately, the spectrum is potentially very complex because the $(4d^{-1}5p^{-1})np$ configuration gives rise to a large number of possible states, and no detailed assignment has been given for the observed structure. The assignment of the shake-up states for XeF_2 is expected to be even more challenging, although it appears that at least some features can be tentatively assigned. In particular, the XeF_2 $4d^{-1}$ shake-up spectrum shows relatively intense structure at much lower excitation energy than atomic Xe. This structure almost certainly arises from shake-up into the unoccupied σ^* valence orbital, which is not present in atomic Xe.

The excitation energy of the lowest-lying feature in Fig. 9 occurs at an energy of ~8 eV relative to $XeF_2(4d_{5/2}^{-1}\ ^2\Delta_{5/2})$, slightly higher than the excitation energy of the corresponding σ_u^* resonance in neutral XeF_2 (7.85 eV).[77] Consideration of the selection rules provides insight into the nature of the shake-up process. In particular, Table III shows two mechanisms for shake-up involving the σ_u^* resonance, along with the valence-shell configuration of XeF_2. In this simple picture, configurations with multiple excitations, as well as vibronic interactions, are ignored. In the normal shake-up process, the 4d electron is excited into the εl_u continuum via a dipole process, and a valence electron is excited into the σ_u^* orbital via a monopole transition. As seen in Table III, the only allowed monopole process is from the $6\sigma_u$ orbital, which would require ~5 eV more energy than excitation from the $5\pi_u$ highest-occupied molecular orbital (HOMO). On the other hand, the conjugate process involving dipole excitation from 4d to σ_u^* and monopole ionization of a valence orbital is allowed for all of the valence orbitals and is likely the dominant shake-up mechanism for these low-energy features. Alternatively, the broad shoulder and peak observed at 14.31 and 15.64 eV excitation energy may result from the normal shake-up process involving the $6\sigma_u$ orbital.

Assignments of the XeF_2 shake-up features above 13 eV in Fig. 9 run into the same difficulties as for Xe, and they must await more detailed theoretical investigations. By analogy with Xe, however, it appears likely that the structure at binding energies of 13 to ~20 eV in Fig. 9 is associated with $XeF_2(4d^{-1}5p^{-1})6p$ and 7p excitation, and that the structure observed between 23 and 28 eV is associated with the $XeF_2(4d^{-1}5s^{-1})ns$ excitations.[11]

C. Auger decay widths

Returning to the $4d^{-1}$ photolines, the core-excited states of Xe^+ resulting from the removal of a 4d electron have sufficient internal energy to undergo single- or double-Auger processes[78] to produce Xe^{2+} or Xe^{3+}, and the situation is expected to be similar for XeF_2. We now focus on the decay processes of the core-excited XeF_2^+ through the consideration of the total decay rate and the Auger electron spectrum. For the latter, we focus on the single Auger processes because the double Auger process is expected to produce slow electrons with energies below 10 eV.

As discussed in Sec. II A, the decay widths for the ligand-field- and spin–orbit-split $4d^{-1}$ states of XeF_2 can be extracted from the widths of the corresponding photoelectron peaks. In atomic Xe,

the $4d_{5/2}^{-1}$ and $4d_{3/2}^{-1}$ widths differ slightly, with the former being slightly larger than the latter (111 ± 3 meV vs 104 ± 3 meV, respectively).[22] Cutler *et al.*[36] reported a corresponding substate dependence to the $4d^{-1}$ widths in XeF_2 at a photon energy of 94 eV. They also presented a model based on the character of the relevant molecular orbitals that rationalized which states had the greatest width. However, their widths for the corresponding $4d^{-1}$ states of atomic Xe were approximately a factor of two larger than those determined in more recent studies.

The present substate-dependent widths extracted from the Xe and XeF_2 $4d^{-1}$ photoelectron spectra are shown in Fig. S3 of the supplementary material for photon energies between 75 and 250 eV. The spectra at lower photon energies are asymmetrically broadened by post-collision interactions, and the present analysis is thus limited to higher energies. Two observations can be made directly from the data. First, as observed by Cutler *et al.*,[36] the widths for XeF_2 are systematically larger than those for atomic Xe. This observation was used by Buth *et al.*[39] as evidence for the contribution of interatomic Coulombic decay (ICD) to the Auger decay mechanism in the xenon fluorides. Second, the peak widths are essentially constant as a function of the photon energy. We also observed constant widths for Xe, which is consistent with the results of Jurvansuu *et al.*,[22] although Ausmees *et al.*[21] previously found a photon energy dependence to the $4d^{-1}$ widths for Xe.

Table I shows the substate-dependent widths obtained by averaging the values determined for photon energies between 140 and 250 eV. As in the case of the Xe data, the present values for the XeF_2 substates are approximately a factor of two smaller than those of Cutler *et al.*[36] However, their discussion of the relative widths of the different XeF_2 substates is consistent with our observations. In particular, the one-electron orbitals associated with the $4d_{5/2}^{-1}\ ^2\Sigma_{1/2}^+$ and $4d_{3/2}^{-1}\ ^2\Pi_{1/2}$ substates have the greatest amount of d_{z^2} character (i.e., along the F–Xe–F axis), and these substates also have the largest widths.

D. Auger processes

The spectra recorded with $\theta = 0°$ at 90, 120, and 150 eV in connection with the shake-up processes also include the Auger spectra for XeF_2. Figure 10 shows the spectrum recorded at 90 eV, in which the Auger electrons are best isolated from the other photoelectron bands. The double ionization threshold for XeF_2 is expected to be ~30 eV, and the highest energy ligand-field- and spin–orbit-split $4d^{-1}$ level is at 72.538 eV, which means that the highest energy Auger electron will have a kinetic energy of ~40 eV. This expectation is consistent with the spectrum in Fig. 10. Note that the sharp peak at 22.459 eV is an impurity line from atomic Xe $4d_{5/2}^{-1}$ photoionization. Although the Xe concentration is small, the XeF_2 Auger intensities are also small, which makes the Xe photoelectron peak look relatively intense by comparison.

The Auger spectrum following 4d ionization of atomic Xe is split into two groups of lines.[24,79] The first lies at kinetic energies between 29.9 and 36.5 eV and corresponds to Xe^{2+} final states with the $\ldots 5s^2 5p^4$ configuration, while the second lies at energies between 19.1 and 24.1 eV and corresponds to final states with the $\ldots 5s^1 5p^5$ configuration. The corresponding XeF_2 $4d^{-1}$ Auger spectrum spans a somewhat larger range of kinetic energies, and the splitting between the two regions is smaller. This observation is consistent with the much broader range in energies of the XeF_2^+ and XeF_2^{2+} outer-valence states, as compared to Xe^+ and Xe^{2+}. The XeF_2 features at kinetic energies between 30 and 40 eV in Fig. 10 most likely correspond to final state configurations with two holes in a combination of the $5\pi_u$, $10\sigma_g$, $3\pi_g$, and $4\pi_u$ orbitals ("outer–outer" states in the language of Ågren[80]), while the higher binding energy

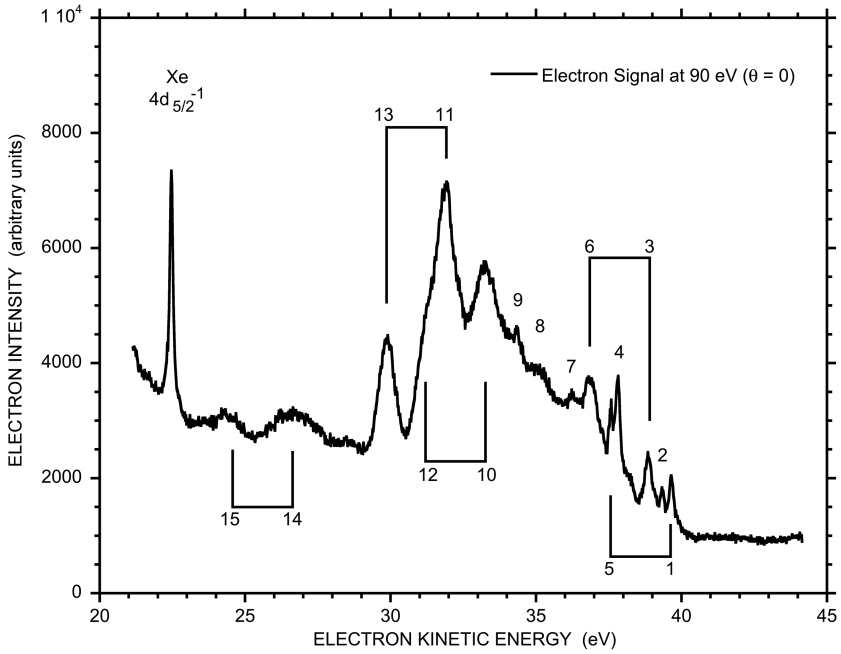

FIG. 10. The Auger electron spectrum recorded at 90 eV photon energy and $\theta = 0°$. The sharp peak at 22.459 eV is from the $4d_{5/2}^{-1}$ photoionization of atomic Xe. The lines connect pairs of peaks separated by the spin–orbit splitting in XeF_2 ($4d^{-1}$), suggesting that they result from the decay into the same final state.

(lower kinetic energy) features may involve configurations with holes in the $6\sigma_u$ (predominantly Xe 5s character) orbitals as well ("outer-inner" states).

As discussed in detail by Buth *et al.*,[38,39] however, the whole molecular orbital picture becomes suspect for the doubly ionized states of XeF_2 as a result of configuration mixing among the two-hole states and three-hole, one-particle states. In addition, the two-hole configurations give rise to a very large number of states very close to the double ionization threshold. For example, Buth *et al.*[39] found 38 electronic states of XeF_2^{2+} within 10 eV of the double ionization threshold and 19 states in the first 5 eV. Thus, the prospects for a detailed assignment without additional theoretical input are not promising. Despite this situation, the Auger spectrum between 23 and 40 eV is actually relatively simple, with only a handful of well-defined features. This observation suggests that there are simplifying aspects to the Auger decay that may ultimately allow for more definitive assignments.

On closer examination, the highest energy Auger line in Fig. 10 occurs at a kinetic energy of 39.71 eV. Assuming that this results from the decay of the XeF_2 $4d_{3/2}^{-1}$ $^2\Pi_{1/2}$ state at 72.538 eV, this kinetic energy corresponds to a double ionization threshold of 32.83 eV. This value is only slightly lower than the double ionization threshold for atomic Xe (33.105 ± 0.004 eV)[24] and somewhat higher than the lowest XeF_2 double ionization potential calculated by Buth *et al.* (30.511 eV)[39] and in reasonably good agreement with the value of Haiduke *et al.* (32.3 eV).[41] The results of Buth *et al.* indicate that the ground state of XeF_2^{2+} can be reasonably well-described as a $^3\Sigma_g^-$ state arising from two holes in the $5\pi_u$ HOMO of the neutral molecule. Note, however, that they calculate two additional $5\pi_u^{-2}$ hole states with $^1\Delta_g$ and $^1\Sigma_g^+$ symmetry within 0.3 eV of the $^3\Sigma_g^-$ state.

If the highest energy Auger peak corresponds to decay from $4d_{3/2}^{-1}$ $^2\Pi_{1/2}$ into the ground state of XeF_2^{2+}, the highest energy Auger peak from a $4d_{5/2}^{-1}$ state will be for the analogous process from the $^2\Sigma_{1/2}$ state, with a kinetic energy of 37.75 eV. Thus, all of the peaks above this kinetic energy must arise from one of the two $4d_{3/2}^{-1}$ states. Unfortunately, even with this limitation, the number of possible final states precludes a definitive assignment. A number of factors add to the difficulty in making detailed assignments for the remainder of the Auger spectrum. First, propensity rules favoring the production of singlet states of the dications of lighter molecules[80,81] are likely to break down for a heavy molecule such as XeF_2. Similarly, while Auger intensities often display site specificity, Buth *et al.*[38] showed that ICD processes contribute ~33% of the total width in the $4d^{-1}$ Auger decay of XeF_2, which makes such arguments somewhat suspect. Finally, although the 4d electrons in XeF_2 are primarily non-bonding, and there is little evidence for vibrational excitation in the singly charged cation, the loss of two valence electrons is more likely to affect the bonding in the doubly charged ion, and thus vibrational excitation is expected to create additional complexity in the Auger electron spectrum.

While not resolution limited, the widths of the $4d_{3/2}^{-1}$ peaks with kinetic energies greater than 37.75 eV are considerably sharper than those with lower kinetic energies (i.e., to those XeF_2^{2+} states with higher internal energy). As discussed in Sec. III E, this does not appear to be a simple case of the lines broadening as a result of an increased number of overlapping transitions. Rather, this observation suggests a faster decay channel for the XeF_2^{2+} sets in about 2 eV above its threshold of formation. Characterization of the ion fragmentation patterns in coincidence with the Auger electrons should be revealing in this regard.

At kinetic energies below ~37.75 eV, the Auger peaks are relatively broad, and the ligand-field-split states are not likely to be resolved. However, for Auger processes from the XeF_2 $4d_{5/2}^{-1}$ and $4d_{3/2}^{-1}$ spin–orbit states that access the same final states, pairs of Auger peaks should be observed that are separated by approximately the ligand-field state-averaged spin–orbit splitting of ~2.01 eV. Several such pairs of peaks are clearly observed in Fig. 10. Table IV gives the energies of the numbered peaks, along with tentative assignments for the spin–orbit symmetry of the initial state in the Auger decay for the paired transitions.

E. Resonant Auger processes

Resonant Auger spectra of XeF_2 were recorded at 61.526, 63.455, and 67.596 eV, corresponding to the (Xe $4d_{5/2}^{-1}$)σ^*, (Xe $4d_{3/2}^{-1}$)σ^*, and (Xe $4d_{5/2}^{-1}$)6pπ resonances, respectively, as well as at two off-resonance energies of 59.50 and 62.60 eV. Spectra were recorded at both $\theta = 0^\circ$ and 90°, allowing the determination of the corresponding β parameters. Figure 11 shows the resonant Auger spectrum recorded at the (Xe $4d_{5/2}^{-1}$)σ^* resonance with $\theta = 90^\circ$ and plotted vs electron binding energy. An expanded version of the region between threshold and 30 eV is shown in the supplementary material, along with the identification of a number of impurity bands due to N_2[82] and O_2.[83] These impurity bands were caused by a very small air leak in the inlet system. While somewhat of a nuisance, these bands allow the accurate calibration of the spectrum and allow the matching of intensities for background subtraction. "Magic-angle" photoelectron spectra and the corresponding β values for the three resonance positions are also provided in the supplementary material.

At binding energies below ~16.5 eV, all of the spectra look quite similar, displaying the $5\pi_u^{-1}$, $10\sigma_g^{-1}$, $3\pi_g^{-1}$, and $4\pi_u^{-1}$ valence

TABLE IV. Auger electron energies and tentative assignments.

Peak number (partner number)[a]	Kinetic energy (eV)	Initial Xe spin–orbit state
1 (5)	39.64	$4d_{3/2}$
2	39.34	$4d_{3/2}$
3 (6)	38.84	$4d_{3/2}$
4	37.83	$4d_{3/2}$
5 (1)	37.58	$4d_{5/2}$
6 (3)	36.87	$4d_{5/2}$
7	36.24	
8	35.12	
9	34.34	
10 (12)	33.24	$4d_{3/2}$
11 (13)	31.89	$4d_{3/2}$
12 (10)	31.25	$4d_{5/2}$
13 (11)	29.88	$4d_{5/2}$
14 (15)	26.64	$4d_{3/2}$
15 (14)	24.27	$4d_{5/2}$

[a]The numbers in parentheses indicate the paired level decaying to the same final state.

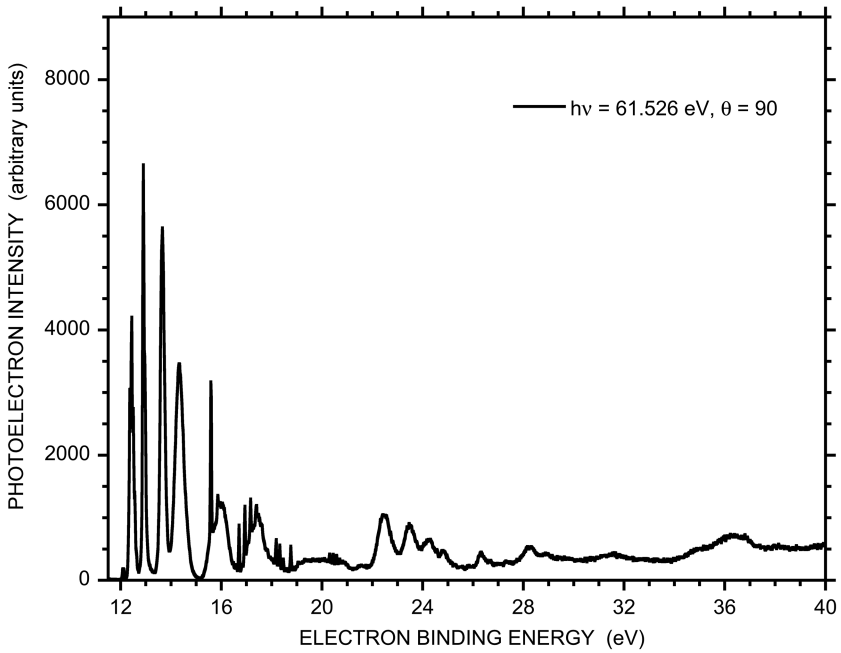

FIG. 11. The resonant Auger spectrum recorded at the $(Xe_{5/2}{}^{-1})\sigma^*$ resonance of XeF_2 at 61.526 eV and plotted vs the electron binding energy. The assignments of the impurity bands are indicated in the supplementary material.

bands resulting from single-photon ionization of the ground state molecule.[84] Magic angle spectra were synthesized using Eq. (6), and these were normalized to each other by using the intensities of the impurity bands. The resulting XeF_2 band intensities on resonance are within 10%–15% of the intensities off resonance, suggesting that the participator Auger processes are relatively weak. This result is consistent with the resonant Auger spectrum of atomic Xe. In particular, the atomic Xe $4d_{5/2}6p$ lifetime width is 0.1098 ± 0.0010 eV,[20] which is very close to the Xe $4d_{5/2}{}^{-1}$ Auger lifetime of 0.111 ± 0.003 eV.[22] This observation suggests that spectator Auger processes will dominate the decay following resonant $(4d^{-1})6p$ excitation in Xe, as is generally found. This result also suggests that spectator decay will dominate in the decay of the $(4d_{5/2}{}^{-1})6p\pi$ resonance in XeF_2 as well. The situation could be somewhat different for the lower-lying $(4d^{-1})\sigma^*$ resonances in XeF_2, but the data below clearly show that spectator decay is the stronger process for these as well.

Above 16.5 eV, a number of new bands are observed in the resonant spectra, along with the usual $6\sigma_u{}^{-1}$ and $9\sigma_g{}^{-1}$ valence bands at 17.39 and 26.28 eV, respectively.[33] To enhance the features in the resonant spectra, we have subtracted the corresponding nonresonant spectrum at 62.50 eV from each of the resonant spectra at $\theta = 0°$ and 90°. Figure 12 shows the resulting 90° difference spectra for the three resonances over the energy range from 16.5 to 40 eV. The signal at the lowest kinetic energies is somewhat noisy because it is overlapped by both the $6\sigma_u{}^{-1}$ band and N_2 and O_2 impurity bands, and the subtraction is imperfect.

The resonant Auger spectra for the XeF_2 $(4d_{5/2}{}^{-1})\sigma^*$ and $(4d_{3/2}{}^{-1})\sigma^*$ resonances show most of the same features between 16.5 and 40 eV, although the relative intensities vary considerably. In contrast, the spectrum recorded on the $(4d_{5/2}{}^{-1})6p\pi$ resonance is quite different. We focus first on the decay of the two σ^* resonances and then contrast this with a discussion of the $6p\pi$ resonance.

The spectator Auger spectra are expected to show strong similarities with the true Auger spectrum. However, because the final state in resonant Auger decay is a singly charged cation rather than a doubly charged cation and because the excited electron is somewhat effective in screening the nuclear charge, the kinetic energies of the peaks are shifted to considerably higher energy than the corresponding peaks in the non-resonant Auger spectrum. The excited electron can also lead to splitting in the Auger peaks depending on the symmetry of the excited orbital, but for the σ^* orbital it is only the spin-splitting, which is expected to be small.

The first few peaks at binding energies of 16.5–18.5 eV in both the $(4d_{5/2}{}^{-1})\sigma^*$ and $(4d_{3/2}{}^{-1})\sigma^*$ resonant Auger spectra bear a striking resemblance to the highest energy features in the true Auger spectrum of Fig. 10. Figure 13 shows an expanded version of the two σ^* spectra, as well as the Auger spectrum, in which the x axis of the latter has been reversed and shifted to line up with the lowest binding energy feature in the σ^* spectra. Note that the Auger spectrum contains contributions from the decay of both the $4d_{5/2}{}^{-1}$ and $4d_{3/2}{}^{-1}$ states of $XeF_2{}^+$, and by plotting in this manner, only the $4d_{3/2}{}^{-1}$ features are expected to line up with the σ^* features. Nevertheless, the overall shapes of the resonant and true Auger spectra appear quite similar. The binding energy with respect to the double ionization threshold of the lowest energy feature in the σ^* spectra is quite substantial. In particular, assuming that the lowest energy spectator Auger feature at 17.09 eV is based on the lowest electronic state of $XeF_2{}^{2+}$, the binding energy is 15.74 eV. This large value reflects the low effective principal quantum number of the σ^* electron (it is effectively a 5p electron).

The similarity between the resonant Auger spectra for the $(4d_{5/2}{}^{-1})\sigma^*$ and $(4d_{3/2}{}^{-1})\sigma^*$ resonances and the regular Auger spectrum extends to the linewidths of the lowest few features in the resonant Auger spectra. While these features are quite sharp, from just 2 eV above the lowest feature, the linewidth appears to increase

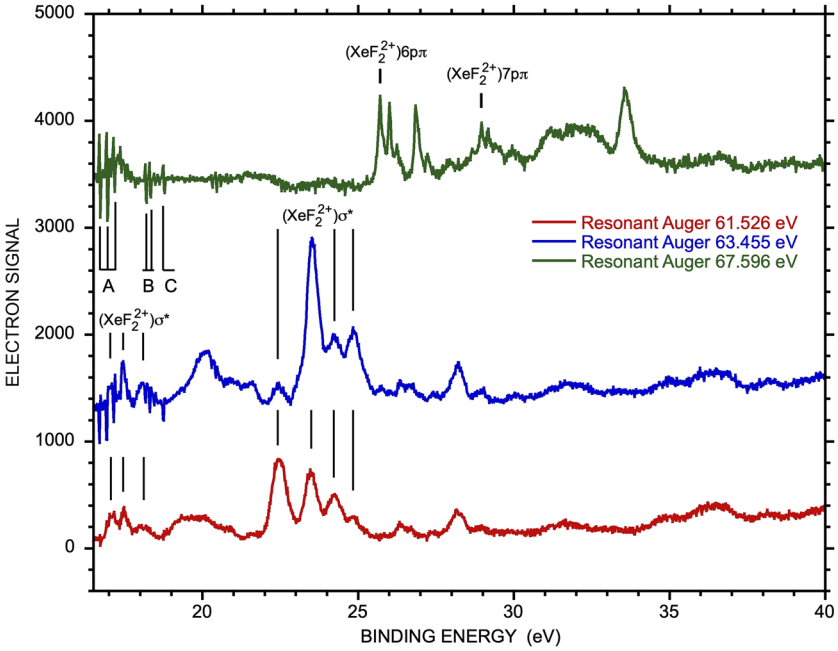

FIG. 12. The difference photoelectron spectra recorded at 90° in which the off-resonance spectrum recorded at 62.50 eV was subtracted from the spectra for the $(4d_{5/2}^{-1})\sigma^*$, $(4d_{3/2}^{-1})\sigma^*$, and $(4d_{5/2}^{-1})6p\pi$ resonances. See the text for details. The sharp spikes labeled A, B, and C correspond to imperfectly subtracted impurity bands corresponding to vibrational levels of the N_2^+ A $^2\Pi_u$, O_2^+ b $^4\Sigma_g^-$, and N_2^+ B $^2\Sigma_u^+$ states, respectively.

substantially. Unlike the regular Auger spectra, the resonant Auger spectra are state selected, and the increased linewidth does not appear to be simply due to an increased density of transitions. This observation suggests that the XeF_2^{2+} ion core of the $(XeF_2^{2+})\sigma^*$ states populated in the resonant Auger decay has similar dissociation/decay dynamics as the free XeF_2^{2+} ion.

The similarity of the $(4d_{5/2}^{-1})\sigma^*$ and $(4d_{3/2}^{-1})\sigma^*$ spectra between 16.5 and 30 eV suggests that the Auger decay of the corresponding cores accesses the same final states, albeit with different relative intensities. This behavior is extended to the higher-lying states as well. Here, the correspondence with the true Auger spectrum is somewhat less obvious, but a clear similarity remains.

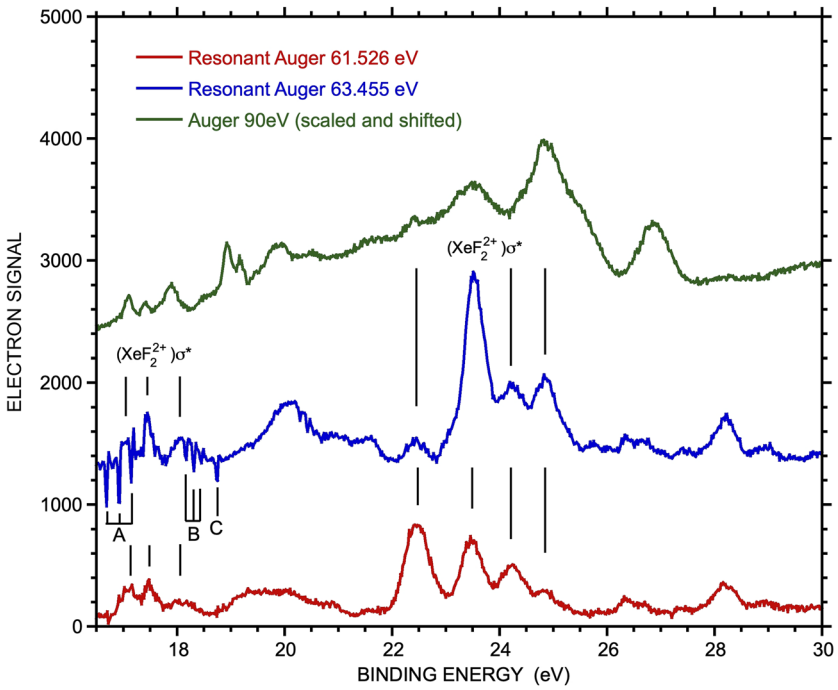

FIG. 13. Expanded portions of the $(4d_{5/2}^{-1})\sigma^*$ and $(4d_{3/2}^{-1})\sigma^*$ spectra from Fig. 12, along with the normal $\theta = 0°$ Auger electron spectrum recorded at 90 eV, where the x axis of the latter has been reversed and shifted to line up with the lowest binding energy feature of the σ^* spectra. The sharp spikes labeled A, B, and C correspond to imperfectly subtracted impurity bands corresponding to vibrational levels of the N_2^+ A $^2\Pi_u$, O_2^+ b $^4\Sigma_g^-$, and N_2^+ B $^2\Sigma_u^+$ states, respectively.

Interestingly, some of the higher energy features are significantly stronger than the lowest energy features, suggesting that decay to molecular ion states based on the Xe^{2+} $^1D_2$ and $^1S_0$ states is enhanced relative to those based on the ^3P_J states. As discussed for the Auger spectra, this interpretation is complicated by the large number of low-lying states of the doubly ionized molecule.[39]

The 67.596 eV spectrum of XeF_2 corresponds to excitation of the $(4d_{5/2}{}^{-1})6p\pi$ Rydberg state, and spectator Auger decay is expected to populate the $6p\pi$ Rydberg states converging to low-lying electronic states of $XeF_2{}^+$. For atomic Xe, the lowest lying Xe^{2+} $(^3P_2)6p$ Rydberg state is bound by 7.114 eV relative to the Xe^{2+} $^3P_2$ ground state (33.3397 eV above Xe $^1S_0$). The lowest-lying feature in the XeF_2 $(4d_{5/2}{}^{-1})6p\pi$ resonant Auger spectrum lies at 25.70 eV, or 7.13 eV below the $XeF_2{}^{2+}$ threshold, clearly suggesting a spectator process to a $6p\pi$ state of the singly charged cation. The structure of the lowest lying features in the $6p\pi$ spectrum shows somewhat different splittings than the σ^* spectra, reflecting the coupling of the $6p\pi$ electron with the different ion-core states. Most of the remaining structure in the $6p\pi$ spectrum has splittings of 0.2–0.4 eV, making it unlikely to be vibrational structure, and more likely reflects decay to different $XeF_2{}^{2+}$ states. The features between 25.5 and 27.5 eV are also relatively sharp, which is consistent with the longer lifetimes of the corresponding $(4d^{-1})\sigma^*$ states and the relative stability of these $(XeF_2{}^{2+})6p\pi$ states.

Shake-up processes are often significant in resonant Auger spectra. The lowest $(Xe^{2+})7p$ state has a binding energy of 3.725 eV,[85] while the XeF_2 feature at 28.957 eV has a binding energy of 3.87 eV. This observation strongly suggests an assignment to the lowest $(XeF_2{}^{2+})7p\pi$ Rydberg state, and neighboring features probably reflect additional core states. Not unexpectedly, the two σ^* resonant Auger spectra do not show significant features that match up with the $6p\pi$ and $7p\pi$ features in the $(4d_{5/2}{}^{-1})6p\pi$ spectrum. This result is consistent with the shake-up process preserving the l symmetry of the excited electron. On the other hand, a stronger feature is observed in the σ^* spectra at ~26.32 eV, or 0.62 eV above $6p\pi$ in the $(4d_{5/2}{}^{-1})6p\pi$ spectrum. This feature is likely a result of shake-up from the σ^* into the $6p\sigma$ orbital. Interestingly, Comes *et al.* assigned the $(4d_{5/2}{}^{-1})6p\sigma$ transition to a feature lying ~0.78 eV above the $(4d_{5/2}{}^{-1})6p\pi$ transition, in reasonably good agreement with the present splitting observed in the lower-lying states.

IV. CONCLUSIONS

We have presented an extensive experimental study of the $4d^{-1}$ ionization of XeF_2, including ion-yield curves, and ligand-field- and spin–orbit-resolved photoelectron angular distributions and branching fractions. The overall behavior closely follows the corresponding ion yields, angular distributions, and branching fractions for atomic Xe, and some of the results are reproduced reasonably well by theoretical calculations of the photoionization process. In particular, although the theoretical XeF_2 cross section between the 4d threshold and 250 eV does not agree well with the experiment, the corresponding β values and branching fractions are fairly well reproduced. Ligand-field- and spin–orbit-resolved lifetime widths were also measured for the resulting photoions, and these are consistent with the widths observed for atomic Xe. We also discussed the shake-up processes accompanying photoionization and the Auger electron spectra resulting from the decay of the photoion. Finally, resonant Auger spectra were recorded just below the 4d threshold for the $(4d_{5/2})\sigma^*$, $(4d_{3/2})\sigma^*$, and $(4d_{5/2})6p\pi$ resonances. These spectra show many features in common with the normal Auger spectra. Interestingly, both the Auger and resonant Auger spectra appear to be relatively simple, despite the large number of doubly ionized XeF_2 states close to threshold. Understanding the source of this simplicity is an interesting problem for the future.

The present results suggest a number of future experiments. As shown by Southworth *et al.* at the 3d edge of XeF_2,[35] neutral and ionic fragmentation patterns can provide a different window into the competing decay processes of the primary photoions or resonant levels of the neutral. Second, coincidence measurements of the photoelectron and Auger electron such as those performed on atomic Xe would help to disentangle the Auger spectrum.[15,27,28,74] Finally, comprehensive resonant Auger measurements of a larger set of pre-threshold resonances could provide considerable insight into the Rydberg states of the singly charged cation converging to the doubly charged ion, and into the associated shake-up and shake-down processes. Such comprehensive measurements on prototypical heavy atom systems such as XeF_2 will also help provide a framework for a more detailed analysis of novel time-resolved x-ray studies, such as the recent two-color pump–probe experiments on XeF_2 performed using a free-electron x-ray laser source.[86]

SUPPLEMENTARY MATERIAL

See the supplementary material for a schematic figure of the interaction region, along with additional figures of the energy-dependent Auger widths, and expanded plots of the resonant Auger spectra and magic-angle Auger spectra.

ACKNOWLEDGMENTS

We would like to thank C. Buth and L. Cederbaum for making the digital data from their calculations on the double ionization potentials of XeF_2 available to us and for helping us with their interpretation. D.M.P.H. acknowledges the Science and Technology Facilities Council (United Kingdom) for financial support. S.T.P. was supported by the U.S. Department of Energy, Office of Science, Office of Basic Energy Sciences, Division of Chemical Sciences, Geosciences, and Biosciences, under Contract No. DE-AC02-06CH11357. We are grateful to the SOLEIL staff for running the facility and providing beamtime under Project No. 20190046.

The submitted manuscript has been created by UChicago Argonne, LLC, Operator of Argonne National Laboratory ("Argonne"). Argonne, a U.S. Department of Energy Office of Science laboratory, is operated under Contract No. DE-AC02-06CH11357. The U.S. Government retains for itself, and others acting on its behalf, a paid-up nonexclusive, irrevocable worldwide license in said article to reproduce, prepare derivative works, distribute copies to the public, and perform publicly and display publicly, by or on behalf of the Government.

AUTHOR DECLARATIONS

Conflict of Interest

The authors have no conflicts to disclose.

DATA AVAILABILITY

The data that support the findings of this study are available from the corresponding author upon reasonable request.

REFERENCES

[1]K. Codling and R. P. Madden, Phys. Rev. Lett. **12**, 106 (1964).
[2]A. F. Starace, Phys. Rev. A **2**, 118 (1970).
[3]D. J. Kennedy and S. T. Manson, Phys. Rev. A **5**, 227 (1972).
[4]S. P. Shannon, K. Codling, and J. B. West, J. Phys. B: At. Mol. Phys. **10**, 825 (1977).
[5]G. C. King, M. Tronc, F. H. Read, and R. C. Bradford, J. Phys. B: At. Mol. Phys. **10**, 2479 (1977).
[6]J. B. West and J. Morton, At. Data Nucl. Data Tables **22**, 103 (1978).
[7]K. T. Cheng and W. R. Johnson, Phys. Rev. A **28**, 2820 (1983).
[8]D. J. Bristow, J. S. Tse, and G. M. Bancroft, Phys. Rev. A **25**, 1 (1982).
[9]S. Southworth, U. Becker, C. M. Truesdale, P. H. Kobrin, D. W. Lindle, S. Owaki, and D. A. Shirley, Phys. Rev. A **28**, 261 (1983).
[10]D. W. Lindle, T. A. Ferrett, P. A. Heimann, and D. A. Shirley, Phys. Rev. A **37**, 3808 (1988).
[11]S. Svensson, B. Eriksson, N. Mårtensson, G. Wendin, and U. Gelius, J. Electron Spectrosc. Relat. Phenom. **47**, 327 (1988).
[12]B. Kämmerling, H. Kossman, and V. Schmidt, J. Phys. B: At., Mol. Opt. Phys. **22**, 841 (1989).
[13]U. Becker, D. Szostak, H. G. Kerkhoff, M. Kupsch, B. Langer, R. Wehlitz, A. Yagishita, and T. Hayaishi, Phys. Rev. A **39**, 3902 (1989).
[14]N. Shanthi and P. C. Deshmukh, Phys. Rev. A **40**, 2400 (1989).
[15]B. Kämmerling, B. Krässig, and V. Schmidt, J. Phys. B: At., Mol. Opt. Phys. **23**, 4487 (1990).
[16]T. Hayaishi, E. Murakami, Y. Morioka, H. Aksela, S. Aksela, E. Shigemasa, and A. Yagishita, Phys. Rev. A **44**, R2771 (1991).
[17]W. F. Chan, G. Cooper, X. Guo, G. R. Burton, and C. E. Brion, Phys. Rev. A **46**, 149 (1992).
[18]A. Ausmees, S. J. Osborne, R. Moberg, S. Svensson, S. Aksela, O.-P. Sairanen, A. Kivimäki, A. Naves de Brito, E. Nõmmiste, J. Jauhiainen, and H. Aksela, Phys. Rev. A **51**, 855 (1995).
[19]A. Ausmees, S. J. Osborne, S. Svensson, A. Naves de Brito, O.-P. Sairanen, A. Kivimäki, E. Nõmmiste, H. Aksela, and S. Aksela, Phys. Rev. A **52**, 2943 (1995).
[20]O.-P. Sairanen, A. Kivimäki, E. Nõmmiste, H. Aksela, and S. Aksela, Phys. Rev. A **54**, 2834 (1995).
[21]A. Ausmees, A. Hahlin, S. L. Sorensen, S. Sundin, I. Hjelte, O. Björneholm, and S. Svensson, J. Phys. B: At., Mol. Opt. Phys. **32**, L197 (1999).
[22]M. Jurvansuu, A. Kivimäki, and S. Aksela, Phys. Rev. A **64**, 012502 (2001).
[23]H. Wang, G. Snell, O. Hemmers, M. M. Sant'Anna, I. Sellin, N. Berrah, D. W. Lindle, P. C. Deshmukh, N. Haque, and S. T. Manson, Phys. Rev. Lett. **87**, 123004 (2001).
[24]T. X. Carroll, J. D. Bozek, E. Kukk, V. Myrseth, L. J. Sæthre, T. D. Thomas, and K. Wiesner, J. Electron Spectrosc. Relat. Phenom. **125**, 127 (2002).
[25]F. Penent, J. Palaudoux, P. Lablanquie, L. Andric, R. Feifel, and J. H. D. Eland, Phys. Rev. Lett. **95**, 083002 (2005).
[26]It has been recently proposed to change the name "Auger decay" to "Auger-Meitner decay" to recognize the work of Lise Meitner in the discovery of this effect. See: D. Matsakis, A. Coster, B. Laster, and R. Sime, "A renaming proposal: 'The Auger–Meitner effect,'" Phys. Today **72**(9), 10 (2019).
[27]B. Kämmerling, B. Krässig, and V. Schmidt, J. Phys. B: At., Mol. Opt. Phys. **25**, 3621 (1992).
[28]B. Kämmerling and V. Schmidt, J. Phys. B: At., Mol. Opt. Phys. **26**, 1141 (1993).
[29]J. Viefhaus, S. Cvejanović, B. Langer, T. Lischke, G. Prümper, D. Rolles, A. V. Golovin, A. N. Grum-Grzhimailo, N. M. Kabachnik, and U. Becker, Phys. Rev. Lett. **92**, 083001 (2004).
[30]H. Basch, J. W. Moskowitz, C. Hollister, and D. Hankin, J. Chem. Phys. **55**, 1922 (1971).
[31]F. J. Comes, R. Haensel, U. Nielsen, and W. H. E. Schwarz, J. Chem. Phys. **58**, 516 (1973).
[32]T. X. Carroll, R. W. Shaw, T. D. Thomas, C. Kindle, and N. Bartlett, J. Am. Chem. Soc. **96**, 1989 (1974).
[33]G. M. Bancroft, P. A. Malmquist, S. Svensson, E. Basilier, U. Gelius, and K. Siegbahn, Inorg. Chem. **17**, 1595 (1978).
[34]S. Aksela, G. M. Bancroft, D. J. Bristow, H. Aksela, and G. J. Schrobilgen, J. Chem. Phys. **82**, 4809 (1985).
[35]S. H. Southworth, R. Wehlitz, A. Picón, C. S. Lehmann, L. Cheng, and J. F. Stanton, J. Chem. Phys. **142**, 224302 (2015).
[36]J. N. Cutler, G. M. Bancroft, J. D. Bozek, K. H. Tan, and G. J. Schrobilgen, J. Am. Chem. Soc. **113**, 9125 (1991).
[37]G. M. Bancroft, S. Aksela, H. Aksela, K. Gürtler, K. H. Tan, B. W. Yates, and J. S. Tse, J. Phys. B: At. Mol. Phys. **20**, 3057 (1987).
[38]C. Buth, R. Santra, and L. S. Cederbaum, J. Chem. Phys. **119**, 7763 (2003).
[39]C. Buth, R. Santra, and L. S. Cederbaum, J. Chem. Phys. **119**, 10575 (2003).
[40]M. Pernpointner and L. S. Cederbaum, J. Chem. Phys. **122**, 214302 (2005).
[41]R. L. A. Haiduke, H. de Paiva Martins Filho, and A. B. F. da Silva, Chem. Phys. **348**, 89 (2008).
[42]R. Forbes, A. De Fanis, C. Bomme, D. Rolles, S. T. Pratt, I. Powis, N. A. Besley, S. Nandi, A. R. Milosavljević, C. Nicolas, J. D. Bozek, J. G. Underwood, and D. M. P. Holland, J. Chem. Phys. **149**, 094304 (2018).
[43]R. Forbes, A. De Fanis, D. Rolles, S. T. Pratt, I. Powis, N. A. Besley, A. R. Milosavljević, C. Nicolas, J. D. Bozek, and D. M. P. Holland, J. Phys. B: At., Mol. Opt. Phys. **53**, 155101 (2020).
[44]R. Forbes, A. De Fanis, C. Bomme, D. Rolles, S. T. Pratt, I. Powis, N. A. Besley, M. Simon, S. Nandi, A. R. Milosavljević, C. Nicolas, J. D. Bozek, J. G. Underwood, and D. M. P. Holland, J. Chem. Phys. **149**, 144302 (2018).
[45]C. N. Yang, Phys. Rev. **74**, 764 (1948).
[46]G. M. J. Barca, C. Bertoni, L. Carrington, D. Datta, N. De Silva, J. E. Deustua, D. G. Fedorov, J. R. Gour, A. O. Gunina, E. Guidez, T. Harville, S. Irle, J. Ivanic, K. Kowalski, S. S. Leang, H. Li, W. Li, J. J. Lutz, I. Magoulas, J. Mato, V. Mironov, H. Nakata, B. Q. Pham, P. Piecuch, D. Poole, S. R. Pruitt, A. P. Rendell, L. B. Roskop, K. Ruedenberg, T. Sattasathuchana, M. W. Schmidt, J. Shen, L. Slipchenko, M. Sosonkina, V. Sundriyal, A. Tiwari, J. L. Galvez Vallejo, B. Westheimer, M. Włoch, P. Xu, F. Zahariev, and M. S. Gordon, J. Chem. Phys. **152**, 154102 (2020).
[47]M. W. Schmidt, K. K. Baldridge, J. A. Boatz, S. T. Elbert, M. S. Gordon, J. H. Jensen, S. Koseki, N. Matsunaga, K. A. Nguyen, S. Su, T. L. Windus, M. Dupuis, and J. A. Montgomery, J. Comput. Chem. **14**, 1347 (1993).
[48]S. Reichman and F. Schreiner, J. Chem. Phys. **51**, 2355 (1969).
[49]F. A. Gianturco, R. R. Lucchese, and N. Sanna, J. Chem. Phys. **100**, 6464 (1994).
[50]A. P. P. Natalense and R. R. Lucchese, J. Chem. Phys. **111**, 5344 (1999).
[51]R. R. Lucchese, N. Sanna, A. P. P. Natalense, and F. A. Gianturco, The ePolyScat User's Manual, available at https://epolyscat.droppages.com/.
[52]J. L. Dehmer, D. Dill, and S. Wallace, Phys. Rev. Lett. **43**, 1005 (1979).
[53]P. M. Dittman, D. Dill, and J. L. Dehmer, J. Chem. Phys. **76**, 5703 (1982).
[54]J. R. Swanson, D. Dill, and J. L. Dehmer, J. Phys. B: At. Mol. Phys. **14**, L207 (1981).
[55]I. Powis, Phys. Rev. A **84**, 013402 (2011).
[56]P. Hockett, XeF_2 4d photoionization calculations, OSF, 2021, available at https://doi.org/10.17605/OSF.IO/JWYP7.
[57]M. Ya. Amusia and J.-P. Connerade, Rep. Prog. Phys. **63**, 41 (2000).
[58]Y.-J. Chen, S. Pabst, and R. Santra, J. Phys. Commun. **2**, 045024 (2018).
[59]P. Hockett and K. L. Reid, J. Chem. Phys. **127**, 154308 (2007).
[60]P. Hockett, *Photoionization Dynamics of Polyatomic Molecules* (University of Nottingham, 2009), available at http://eprints.nottingham.ac.uk/10857/.
[61]Y. Hikosaka, P. Lablanquie, F. Penent, T. Kaneyasu, E. Shigemasa, J. H. D. Eland, T. Aoto, and K. Ito, Phys. Rev. Lett. **98**, 183002 (2007).
[62]K. Codling and R. P. Madden, Appl. Opt. **4**, 1431 (1965).
[63]B. W. Yates, K. H. Tan, G. M. Bancroft, L. L. Coatsworth, J. S. Tse, and G. J. Schrobilgen, J. Chem. Phys. **84**, 3603 (1986).
[64]J. S. Tse, J. Chem. Phys. **89**, 920 (1988).
[65]G. B. Armen, J. Tulkki, T. Åberg, and B. Crasemann, Phys. Rev. A **36**, 5606 (1987).
[66]J. A. R. Samson, W. C. Stolte, Z. X. He, J. N. Cutler, and D. Hansen, Phys. Rev. A **54**, 2099 (1996).

[67]S. Kosugi, M. Iizawa, Y. Kawarai, Y. Kuriyama, A. L. D. Kilcoyne, F. Koike, N. Kuze, D. S. Slaughter, and Y. Azuma, J. Phys. B: At., Mol. Opt. Phys. **48**, 115003 (2015).
[68]K.-N. Huang, W. R. Johnson, and K. T. Cheng, At. Data Nucl. Data Tables **26**, 33 (1981).
[69]E. Kukk, J. D. Bozek, J. A. Sheehy, P. W. Langhoff, and N. Berrah, J. Phys. B: At., Mol. Opt. Phys. **33**, L51 (2000).
[70]J. W. Cooper, Phys. Rev. **128**, 681 (1962).
[71]J. Cooper and R. N. Zare, J. Chem. Phys. **48**, 942 (1968); Erratum **49**, 4252 (1968).
[72]I. Powis, D. M. P. Holland, E. Antonsson, M. Patanen, C. Nicolas, C. Miron, M. Schneider, D. Yu. Soshnikov, A. Dreuw, and A. B. Trofimov, J. Chem. Phys. **143**, 144304 (2015).
[73]D. M. P. Holland, S. Nandi, C. Nicolas, J. D. Bozek, M. Patanen, and I. Powis, Chem. Phys. **542**, 111050 (2021).
[74]V. Schmidt, *Electron Spectrometry of Atoms Using Synchrotron Radiation* (Cambridge University Press, Cambridge, UK, 1997).
[75]J. S. Tse, D. J. Bristow, G. M. Bancroft, and G. Schrobilgen, Inorg. Chem. **18**, 1766 (1979).
[76]D. M. P. Holland, private communication (2021).
[77]U. Nielsen and W. H. E. Schwarz, Chem. Phys. **13**, 195 (1976).
[78]N. Saito and I. H. Suzuki, Int. J. Mass Spectrom. Ion Process. **115**, 157 (1992).
[79]J. Söderström, A. Lindblad, A. N. Grum-Grzhimailo, O. Travnikova, C. Nicolas, S. Svensson, and C. Miron, New J. Phys. **13**, 073014 (2011).
[80]H. Ågren, J. Chem. Phys. **75**, 1267 (1981).
[81]H. Ågren and O. Vahtras, J. Phys. B: At., Mol. Opt. Phys. **26**, 913 (1993).
[82]P. Baltzer, M. Larsson, L. Karlsson, B. Wannberg, and M. Carlsson Göthe, Phys. Rev. A **46**, 5545 (1992).
[83]O. Edqvist, E. Lindholm, L. E. Selin, and L. Åsbrink, Phys. Scr. **1**, 25 (1970).
[84]C. R. Brundle, M. B. Robin, and G. R. Jones, J. Chem. Phys. **52**, 3383–3386 (1970).
[85]NIST Atomic Spectra Database at https://physics.nist.gov/cgi-bin/ASD/levels_hold.pl?el=Xe.
[86]A. Picon, C. S. Lehmann, C. Bostedt, A. Rudenko, A. Marinelli, T. Osipov, D. Rolles, N. Berrah, C. Bomme, M. Bucher, G. Doumy, B. Erk, K. R. Ferguson, T. Gorkhover, P. J. Ho, E. P. Kanter, B. Krassig, J. Krzywinski, A. A. Lutman, A. M. March, D. Moonshiram, D. Ray, L. Young, S. T. Pratt, and S. H. Southworth, Nat. Commun. **7**, 11652 (2016).